

Department of Physics and Astronomy
University of Heidelberg

Bachelor Thesis in Physics
submitted by

Felix Reidt

born in Schwetzingen

2010

Development and Implementation of a Diffractive-Gap Trigger for the ALICE TRD Pre-Trigger System

This Bachelor Thesis has been carried out by Felix Reidt at the
Physikalisches Institut at the University of Heidelberg
under the supervision of
Prof. Dr. Johanna Stachel

Development and Implementation of a Diffractive-Gap Trigger for the ALICE TRD Pre-Trigger System

In order to study central diffractive events with the ALICE experiment, a trigger for the Central Trigger Processor of ALICE is required. Central diffractive events are characterized by gaps in pseudo-rapidity separating the centrally produced system from the beam particle remnants. The Pre-Trigger System of the Transition Radiation Detector is able to derive the required gap information from the fast T0 and V0 detectors. The presence of a centrally produced system can be detected by the Time-of-Flight detector. This information about the gaps and the centrally produced system has to be processed within the L0 time window of 800 ns. In this thesis the development of the TRD Pre-Trigger System simulation environment in AliRoot is described. Moreover, the simulation environment is used to study the feasibility of a diffractive-gap trigger for the identification of central diffractive and the rejection of minimum bias events. The central diffractive events are generated by Phojet whereas Pythia8 is used to simulate the background.

Entwicklung und Implementierung eines diffraktiven Gap-Triggers für das ALICE TRD Pre-Trigger System

Um zentrale diffraktive Ereignisse im ALICE-Experiment zu studieren, wird ein Trigger für den zentralen Trigger Prozessor benötigt. Zentrale diffraktive Ereignisse werden charakterisiert durch Pseudo-Rapidityslücken, die das zentral erzeugte System und die Zerfallsprodukte der Strahlteilchen trennen. Das Pre-Trigger-System des Übergangsstrahlungs-Detektors kann die benötigten Informationen über die Lücken von den schnellen T0 und V0 Detektoren erlangen. Das Vorhandensein eines zentral erzeugten Systems kann vom Flugzeit-Detektor festgestellt werden. Diese Information muss rechtzeitig innerhalb des L0 Zeitfensters von 800 ns verarbeitet werden. Im Rahmen dieser Arbeit wird die Entwicklung der Simulationsumgebung für das TRD Pre-Trigger System in AliRoot beschrieben. Desweiteren wird die Simulationsumgebung genutzt, um die Machbarkeit eines diffraktiven Gap Triggers zur Identifikation von zentralen diffraktiven Ereignissen und zur Unterdrückung von Minimum-Bias-Ereignissen zu studieren. Die zentral-diffraktiven Ereignisse werden mit Phojet erzeugt, wohingegen Pythia8 genutzt wird, um den Untergrund zu simulieren.

Contents

1. Introduction	1
2. Diffraction	3
2.1. Total Cross-Sections	3
2.2. Regge theory	4
2.3. Diffractive Topologies	5
2.4. Central Diffraction Measurements	6
3. ALICE	11
3.1. Central Detectors	11
3.2. Forward Detectors	13
3.3. Trigger System	15
3.4. Acceptance in Pseudo-Rapidity	15
3.5. ALICE Studies on Central Diffraction	15
4. TRD Pre-Trigger Simulation Environment	17
4.1. TRD Pre-Trigger System Overview	17
4.2. Software Description	19
4.2.1. AliRoot	19
4.2.2. Class to Hardware Component Assignment	20
4.2.3. Class Descriptions	20
4.3. Configuration Files	24
5. Diffractive-Gap Trigger Evaluation	27
5.1. Monte Carlo Event Generator Selection	27
5.2. Diffractive Cross Sections	29
5.3. Definition of a Gap Trigger	29
5.4. Trigger Evaluation Minimum Bias Events	29
5.5. Trigger Evaluation Central Diffractive Events	33
5.6. Trigger Evaluation Summary	36
6. Summary and Outlook	39
A. Acronyms and Technical Terms	41
B. Pre-Trigger Configuration File	43
Bibliography	51

1. Introduction

The Standard Model describes three of the four interactions at the quantum level, the weak force, the hadronic force and the electromagnetic force. The Standard Model contains all of today's knowledge on elementary particles and their interactions. It presents a unified picture of the strong, weak and electromagnetic interactions which are formulated as gauge theory. Of these interactions, the hadronic force is the least well understood. Quantum Chromodynamics (QCD), the theory of the strong interactions, describes the strong force by the exchange of colored gluons. The color charge of the gluons leads to two particular properties of QCD, confinement and asymptotic freedom [1, 2]. A deconfined state is expected to exist at temperatures and energy densities far away from the ground state. ALICE (**A Large Ion Collider Experiment**) is optimized to explore this deconfined matter, the Quark-Gluon Plasma (QGP) which is presumed to have existed about $10 \mu\text{s}$ after the big bang. It is the state of matter above a critical temperature and density in which the quarks and gluons are freed from their confinement into hadrons. The only way to reproduce this state in the laboratory is the collision of heavy nuclei at high energies. The **Large Hadron Collider** (LHC) at the CERN (Conseil Européen pour la Recherche Nucléaire) can produce these collisions with a maximum energy of 5.5 TeV per nucleon pair.

There are seven experiments at the LHC, the world's most complex hadron collider machine. They investigate the many intriguing aspects of contemporary high-energy particle physics. Besides **A Large Ion Collider Experiment** (ALICE), the LHCb experiment is designed to observe CP violation in B-meson systems. ATLAS (A Toroidal LHC Apparatus) and CMS (Compact Muon Solenoid) are searching for the Higgs boson and new physics like supersymmetric particles and extra dimensions. Even though these two experiments have similar physics objectives, they are using complementary detector technologies. TOTEM studies forward particles in order to measure the total elastic and diffractive cross section. LHCf uses the LHC as a source to study cosmic rays in laboratory conditions. MoEDAL, which is the latest approved experiment, searches for exotic particles like magnetic monopoles or massive stable supersymmetric particles.

QCD has a complex structure due to the color charge of the gluon. The strong force can be mediated by gluon exchange with color charge or by multi-gluon exchange in color-singlet state, i. e. with no color exchange. Strong interactions in the form of color-singlet exchange are known as diffractive processes. Diffractive reactions have been measured at different energies at the Intersecting Storage Rings (ISR), the Super Proton-Antiproton Synchrotron (Sp \bar{p} S), HERA and the Tevatron. Such measurements have contributed in a partially QCD-based formulation of certain diffractive reaction channels. The measurement of central diffraction channels is

experimentally easier accessible than measurements of diffractive dissociation which is very forward-peaked. Central diffractive reaction processes with an intrinsic scale larger than the QCD scale Λ_{QCD} are calculable within QCD. Such measurements offer therefore the prospect of studying the QCD-based formulation of diffraction. Central exclusive production is dominated by multi-gluon fusion in color-singlet state, hence an enhanced production cross section of bound gluonic states is expected. Not much is known about glueballs; good evidence exists only for a scalar glueball, which is the lightest one. The evidence for pseudoscalar and tensor glueballs is only weak, hence the experimental confirmation of such states is of high interest. ALICE has the potential to study central diffractive production of such states, since it provides measurements of low transverse momenta combined with excellent particle identification.

The thesis is structured as follows. Chapter 2 introduces diffraction and discusses in particular central diffraction. The conceptual design and the capabilities of the ALICE detector are depicted in chapter 3. The TRD pre-trigger as well as the corresponding simulation environment are explained in chapter 4. The diffractive-gap trigger evaluation is described in detail in chapter 5. Chapter 6 gives a summary and an outlook.

2. Diffraction

In this chapter some basic concepts as well as the historical background of diffraction are presented. In particular, central diffraction is discussed. Moreover an overview on possible studies in ALICE on the global properties and resonance production of central diffraction is given.

2.1. Total Cross-Sections

Until nearly fifty years ago, it was assumed that the total hadronic cross section reaches asymptotically a constant. Later experiments proved this assumption to be wrong. The first signals came from preliminary $\pi^\pm p$ and $K^\pm p$ scattering data of the Serpukhov machine, a clear evidence was provided by ISR and FNAL experiments. A review on these measurements is given in [3]. In later measurements the UA4 and UA5 experiments at the Super Proton Synchrotron (SPS) at Conseil Européen pour la Recherche Nucléaire (CERN) showed the asymptotic equality of $\sigma_{tot}(pp)$ and $\sigma_{tot}(p\bar{p})$. This asymptotic equality is predicted by the Pommeranchuk theorem. An overview of the measured cross sections together with a fit of the form $(\ln s)^\gamma$ is shown in figure 2.1.

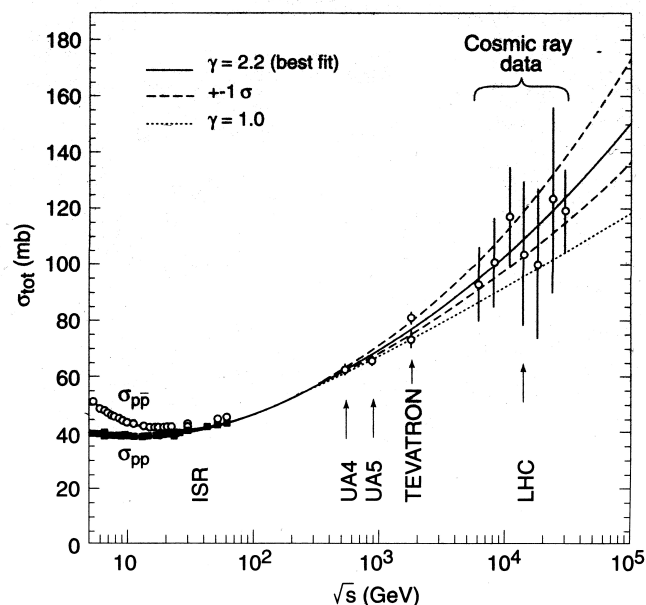


Figure 2.1.: pp and $p\bar{p}$ cross sections, taken from [4]

In order to explain the rise of the total cross sections, Chew and Frautschi (1961) and Gribov (1961) introduced the Pomeron within the framework of Regge theory.

2.2. Regge theory

Regge theory was originally formulated in the context of non-relativistic quantum mechanics. Its very basic idea is the extension of the angular momentum to complex values. The bound states of an attractive, spherically symmetric potential fall into families with increasing angular momentum and energy. These bound states appear as poles of the partial wave amplitude. For well-behaved potentials, these so-called Regge poles follow the equation $l = a(t)$ and they are interpolated by an equation $\alpha(t) = \alpha(0) + \alpha' t$, the Regge trajectory. Here, $\alpha(0)$ and α' are the intercept and the slope, respectively.

In Coulomb scattering, the interaction is mediated by a virtual photon exchanged in the t-channel and analogously strong interactions can be mediated by the t-channel exchange of mesons, as shown in figure 2.2.

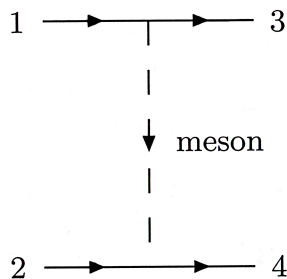


Figure 2.2.: Exchange of a single meson in the t-channel, taken from [5]

The Pomeron, however, is not a particle but a Regge trajectory that is exchanged through the t-channel.

While for leading mesonic trajectories, the ones with the largest intercept, $\alpha(0)$ is about 0.5, the pomeron intercept is slightly above 1. Furthermore the slope differs by about a factor of 4. α' of a mesonic trajectory is of the order of 1 GeV^{-2} , whereas the pomeron slope is assumed to be approximately 0.25 GeV^{-2} , based on elastic scattering data.

Figure 2.3a shows the leading mesonic Regge trajectories and the bound states on the mesonic trajectories are f_2 , ρ , ω and a_2 . An overview on the properties of these particles is given in table 2.1. The Pomeron trajectory is plotted in figure 2.3b with $\alpha_{\mathbb{P}}(t) = 1.08 + 0.25 t \text{ GeV}^{-2}$. The physical states lying on the Pomeron trajectory are assumed to be bound gluonic states.

The description of the Pomeron itself as well as the color-neutral gluonic bound states which are assumed to define the pomeron trajectory, are a challenge for QCD. The data point plotted in figure 2.3b is a candidate for such a glueball. The Pomeron has to be described by the exchange of multiple gluons fulfilling the condition that no quantum numbers except those of the vacuum are exchanged. This is possible through an exchange of color singlets, consisting of at least two gluons.

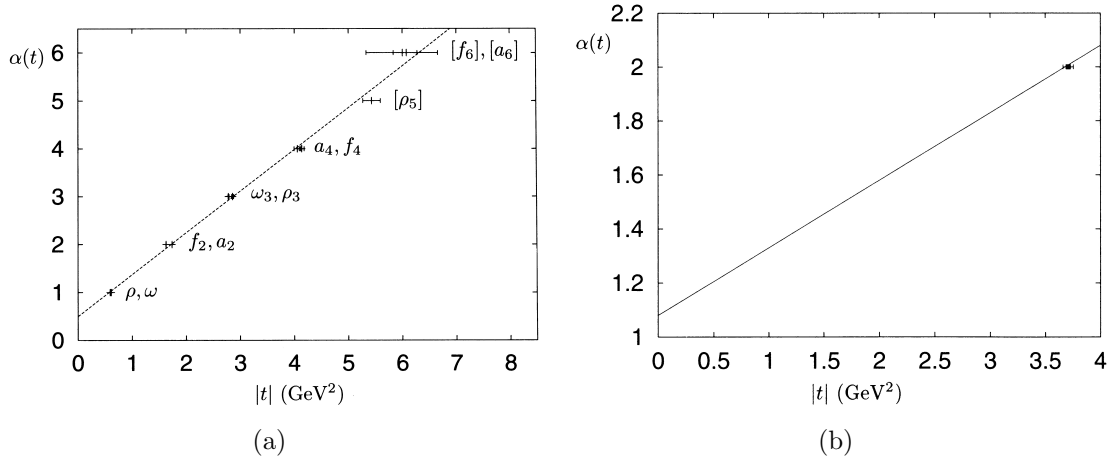


Figure 2.3.: (a) Leading mesonic Regge trajectories, (b) Pomeron trajectory, both taken from [5]

state	P	C	G	I	ξ
f_2	+1	+1	+1	0	+1
ρ	-1	-1	+1	1	-1
ω	-1	-1	-1	0	-1
a_2	+1	+1	-1	1	+1
\mathbb{P}	+1	+1	+1	0	+1

Table 2.1.: Quantum numbers (parity, charge conjugation, G-parity, isospin and signature) of particles on the mesonic and pomeron trajectory

Within Regge theory, the exchange of a trajectory leads to an energy dependence of the corresponding cross section of the form $\sigma \sim s^{\alpha(0)-1}$. Such a form results in a cross section decreasing or increasing in energy for intercepts smaller or larger than one, respectively. The energy dependence of the total hadronic cross section as shown in figure 2.1 can hence be understood to result from a combination of exchanges of Regge and Pomeron trajectories shown in figure 2.3.

2.3. Diffractive Topologies

Diffractive processes are reactions at high energies without an exchange of quantum numbers between the colliding particles [5]. Such interactions can be mediated by an exchange of a Pomeron. Diffractive processes can be distinguished from non-diffractive by the existence of rapidity gaps. The topologies in pseudo-rapidity are outlined in figure 2.4. While particles produced in non-diffractive processes (ND) fill all of pseudo-rapidity space, a rapidity gap is formed in Single Diffractive Dissociation (SD) and Double Diffractive Dissociation (DD). In diffractive dissociative events at least one of the colliding particles breaks up into a bunch of final particles. The variable $\xi = M_X^2/s$ quantifies the fraction of the center-of-mass energy which is used to excite the diffractive state X of mass M_X . This energy is taken from the kinetic energy of the colliding protons, hence by energy-momentum

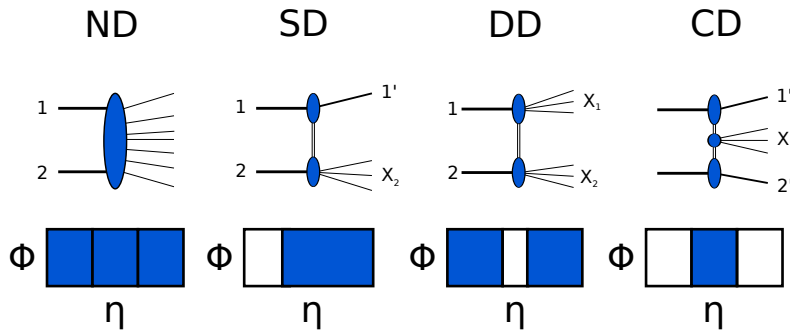


Figure 2.4.: Different diffractive topologies

conservation it follows that $\Delta\eta = -\ln \xi$, with $\Delta\eta$ representing the pseudo-rapidity gap. The width of the pseudo-rapidity gap can therefore be determined by measuring the fractional momentum loss of the intact beam particle. Since this fractional momentum loss is on the order of a few percent or a fraction thereof, this intact particle is very much forward scattered. The measurement of such particles requires the positioning of detectors very close to the beam. The TOTEM, CMS and ATLAS collaborations follow this approach by having Roman-Pot detectors at distances of 220 m and 420 m away from the interaction point.

A central diffractive event is characterized by a large rapidity gap on both sides of central rapidity. This signature hence differentiates central diffraction from diffractive dissociation. Two Pomeron fusion leads to central diffraction. In these events, one or both protons can break up and the rapidity gap can hence be partially filled. Double-Pomeron fusion can be modeled within QCD by two gluon fusion with a third gluon exchanged for shielding the color of the two interacting gluons. The corresponding diagram is shown in figure 2.5.

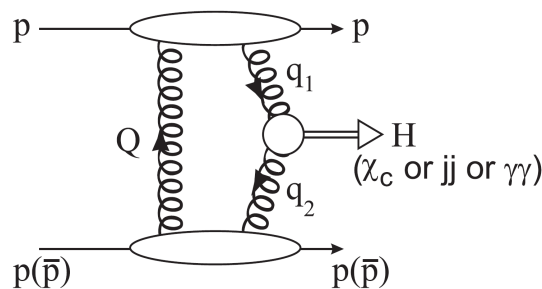


Figure 2.5.: Schematic diagram for central production, taken from [6]

2.4. Central Diffraction Measurements

Low-mass central diffraction measurements are very interesting in the physicists' point of view because these processes provide higher cross sections than the high-

mass ones and so allow systematic studies of central production mechanisms.

The global properties of central diffractive events like the invariant mass spectrum, multiplicity distribution and transverse-momentum distribution can be studied in comparison to minimum-bias events when the rapidity-gap condition is not fulfilled. The slope of the pomeron trajectory $\alpha' = 0.25 \text{ GeV}^{-2}$ is, in comparison to the slope of mesonic trajectories, much smaller. This slope causes a mean k_t in the pomeron wave function of probably above 1 GeV ($\alpha' \sim 1/k_t^2$). Due to this value of k_t , the p_T distribution of the secondary particles in double pomeron exchanges should significantly differ from the one of secondaries from minimum bias events. In particular, the expectation value of the transverse momentum should be larger than in inelastic hadronic events. Furthermore, the $k_t > 1 \text{ GeV}$ implies a large effective temperature which should influence the K/π , η/π , η'/π ratios, resulting in similar production cross sections. The purity of central diffractive events can be checked by analyzing the ρ resonance. Production of the ρ resonance is a very strong signal in hadronic inelastic events but is absent in Pomeron-Pomeron fusion due to the quantum numbers of the ρ ($J^{PC} = 1^{--}$).

Figure 2.6 shows a $\pi^+\pi^-$ invariant-mass spectrum measured at the ISR. While at

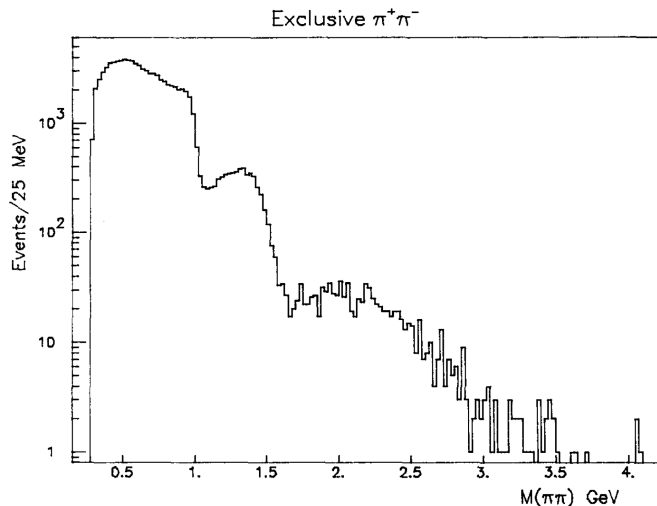


Figure 2.6.: Invariant Mass Spectrum of $\pi^+\pi^-$ at $\sqrt{s} = 63 \text{ GeV}$ measured by the ISR collaboration, taken from [7]

low masses, the $f_0(600) = \sigma$, the lack of ρ and the structure caused by the $f_0(980)$ are well understood, everything beyond is not and could be further investigated by ALICE.

These structures are suspected to be at least partially produced by glueballs. The central exclusive production process of resonances like χ_C and glueballs has an enhanced cross section at LHC as compared to the ISR and SPS energies. Masses of the glueballs are predicted with the help of anisotropic lattice QCD calculations [8]. The lightest three states emerge as the scalar ($J^{PC} = 0^{++}$) with a mass of about $1710 \text{ MeV}/c^2$, tensor ($J^{PC} = 2^{++}$) weighing $\sim 2390 \text{ MeV}/c^2$ and the pseudoscalar ($J^{PC} = 0^{-+}$) with an invariant mass of about $2560 \text{ MeV}/c^2$. An overview of the

experimental status of glueballs can be found here [9].

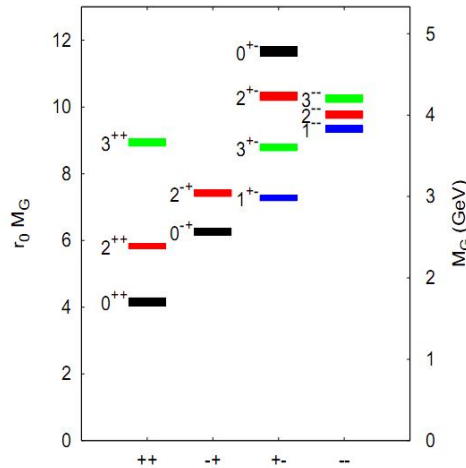


Figure 2.7.: The mass spectrum of glueballs with corresponding J^{PC} , taken from [8]

The central exclusive production of the χ_c is a standard candle for testing the QCD based formalism of central production. This process is described by the Durham-Model trying to close the gap between perturbative models and soft-scale pomeron descriptions [6]. A corresponding Feynman diagram is shown in figure 2.8. In comparison to figure 2.5 this model includes a Sudakov factor as well as suppression factors concerning eikonal and enhanced survival factor and gluon-gluon fusion with unintegrated gluon densities. The interacting gluons emitted from the beam particles are drawn here as two gluon ladders.

The χ_c is a p-wave spin triplet resulting in three states χ_{c0} , χ_{c1} , χ_{c2} with masses, decay widths and branching ratios as shown in table 2.2.

At center-of-mass energies of $\sqrt{s} = 14$ TeV, a central exclusive production cross section of $d\sigma_{excl}/dy|_{y=0} = 45$ nb is predicted [10]. This would result in 4.5×10^5 χ_{c0} in 10^6 s, a bit less than twelve days. The detection efficiency has already been studied in Monte-Carlo simulations and preliminary estimates have been done including the reconstruction efficiency [12]. At the moment about 30 reconstructed $\chi_{c0} \rightarrow p\bar{p}$

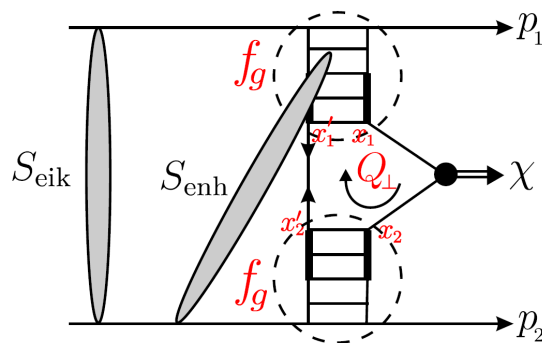


Figure 2.8.: Perturbative mechanism for the central exclusive process $pp \rightarrow p + \chi + p$, taken from [10]

	Mass [MeV]	Width [MeV]	Branching Ratios				
			$J/\Psi\gamma$	$\pi^+\pi^-$	K^+K^-	$p\bar{p}$	$\Lambda\bar{\Lambda}$
χ_{c0}	3415	10	0.01	7×10^{-3}	6×10^{-3}	2×10^{-4}	4×10^{-4}
χ_{c1}	3510	1	0.36	-	-	7×10^{-5}	2×10^{-4}
χ_{c2}	3556	2	0.2	2×10^{-3}	8×10^{-4}	7×10^{-5}	3×10^{-4}

Table 2.2.: χ_c comparison table including masses, widths and branching ratios [11]

decay	Br	4π final states
$\chi_{c0} \rightarrow \pi^+\pi^-$	7×10^{-3}	3.2×10^3
$\chi_{c0} \rightarrow K^+K^-$	6×10^{-3}	2.7×10^3
$\chi_{c0} \rightarrow J/\Psi\gamma$	1×10^{-2}	4.5×10^3
$\chi_{c0} \rightarrow p\bar{p}$	2×10^{-4}	90

Table 2.3.: Overview on χ_{c0} decay channels and branching ratios with the corresponding number of decays in 10^6 s

decays including $\sim 32\%$ efficiency due to PID cuts are estimated. This decay is the one with the lowest branching ratio, but also estimated to be the one with the smallest background, as pointed out in table 2.2, and so the most favorable one.

The fact that there are three χ_c states with similar masses raises the question whether these three states can experimentally be resolved. Preliminary estimates indicate that at least χ_{c0} can be distinguished from χ_{c2} .

The amplitude for color-singlet exchange is characterized by a part which is even under C-parity transformation and a part which is odd. Whereas the C-even part is represented by the Pomeron, the C-odd part is attributed to the Odderon. The C-odd part of the color-singlet amplitude must consist of at least three gluons. Despite numerous searches, the experimental evidence for the Odderon is so far only weak and consists of a deviation measured in pp and $p\bar{p}$ scattering [13]. Central exclusive production of vector mesons therefore opens a new way in the search for Odderon signatures. Diffractive J/Ψ production can take place by Pomeron-photon or Pomeron-Odderon processes with dominance of the photon channel as compared to the Odderon channel. The two production mechanisms result in different p_T distributions of the J/Ψ , hence a careful analysis of the measured p_T distribution might result in an extraction of the Odderon contribution.

Another method to find the Odderon is the measurement of the interference of C-even and C-odd amplitudes resulting in asymmetries of $\pi^+\pi^-$ and K^+K^- pairs. Such asymmetries for example of the polar angle of the π^+ (K^+) in the dipion (dikaon) rest frame have been estimated to be on the order of 10% - 15% for HERA kinematics [14]. Corresponding studies at LHC energies have so far not been carried out.

3. ALICE

In this chapter the subdetectors in the ALICE experiment are described [15]. The detectors in the so-called central barrel cover a pseudo-rapidity range of $|\eta| < 0.9$. The positive and negative pseudo-rapidity ranges are called A and C side, respectively.

While the detectors in the forward region are mainly used for triggering purposes, the ones in the central barrel are used for tracking and particle identification. Since ALICE focuses on Pb-Pb collisions in order to investigate the QGP, it has to deal with a very high multiplicity of charged particles. The LHC is by design capable to accelerate Pb ions to a maximum energy of 2.76 TeV and for this center-of-mass energy a maximum charged-particle multiplicity density of $dN_{ch}/d\eta = 8000$ was assumed during the design phase of ALICE. According to more recent predictions the maximum expected multiplicity density is about $dN_{ch}/d\eta = 3000$ [16].

3.1. Central Detectors

Inner Tracking System

The main tasks of the Inner Tracking System (ITS) are the localization of the primary vertex with an accuracy better than $100 \mu\text{m}$ and the reconstruction of secondary vertices from the decays of hyperons and D and B mesons. Furthermore, the ITS tracks and identifies particles with a momentum less than $200 \text{ MeV}/c$. This improves the angle and momentum resolution for particles reconstructed by the Time-Projection Chamber (TPC) described below and is used in dead regions of the TPC.

The ITS surrounds the beam pipe and consists of 6 coaxially arranged sub-detector layers located at radii between 4 cm and 43 cm. The rapidity range of $|\eta| < 0.9$ is covered by all these layers, but the innermost layer additionally covers the range $|\eta| < 1.98$ to provide a continuous coverage for the measurement of charged particles together with the Forward Multiplicity Detector (FMD), which is described below.

Due to the expected high particle density in heavy-ion collisions at LHC and in order to achieve the required impact parameter resolution, Silicon Pixel Detectors (SPD) have been chosen for the inner two layers. They are surrounded by two Silicon Drift Detectors (SDD) layers and the outer two layers are Silicon micro-Strip Detectors (SSD). The segmentation of all six layers is optimized to achieve the best performance in track finding measuring the impact parameters. The four outer layers have analog readout to measure dE/dx in the non-relativistic ($1/\beta^2$)-region for particle identification down to lowest p_T values. Due to the fact that in the extreme low transverse momentum re-

gion the resolution is limited by multiple Coulomb scattering of the particles, the ITS has an effective thickness of less than 8% of X_0 in order to reduce track distortion.

Time Projection Chamber

The Time Projection Chamber TPC is mainly responsible for the tracking in the central barrel. It is optimized to achieve a good momentum resolution for charged particles including two-track separation, particle identification and vertex determination together with the other detectors in the central barrel. The TPC covers a p_T range of about 0.1 GeV/c up to 100 GeV/c with a momentum resolution up to 0.7% for low momentum particles ($p_T = 500$ MeV/c) in cooperation with the ITS. Except for dead regions at readout chamber boundaries the TPC covers the full azimuthal range. The phase space covered by the TPC in pseudo-rapidity is $|\eta| < 0.9$ for tracks with full radial length. At a third of the radial track length it is possible to achieve a pseudo-rapidity acceptance of $|\eta| < 1.5$ with reduced momentum resolution.

At the Pb-Pb luminosity the LHC is designed for, an interaction rate of 8 kHz with about 10% central collisions is expected. During the design phase a particle multiplicity density of $dN_{ch}/d\eta = 8000$ was assumed, which would result in 20000 charged primary and secondary tracks. By design the TPC can operate at central collision rates of up to 300 Hz in Pb-Pb runs [17].

In proton-proton runs the limiting factor for the luminosity is not the particle multiplicity density but the drift time of about 90 μ s. Already at a pp luminosity of 5×10^{30} cm⁻²s⁻¹ with a corresponding interaction rate of ~ 350 kHz, the TPC measures the tracks of about 60 events together with a triggered event. The occupancy with charged particles is about 30 minimum-bias pp events, but more than a magnitude lower as in Pb-Pb collisions. Tracks of these pile-up events lying in the past or future can be recognized in the offline analysis. A maximum readout rate of over 1400 Hz is possible for p-p collisions [17].

Transition Radiation Detector

The Transition Radiation Detector (TRD) is located in between TPC and Time-of-Flight detector (TOF) at radii between 2.9 m and 3.68 m and covers an azimuthal range of 360° and a pseudo-rapidity of $|\eta| < 0.84$. Its main task is the identification of electrons for momenta above 1 GeV/c. In this momentum range, transition radiation from electrons passing a radiator can be used to differentiate between electrons and pions. Lower momentum electrons can be identified by the TPC.

The TRD consists of 540 gaseous detectors, which have a multiwire proportional chamber on top of a radiator. The TRD was designed to enhance the recorded Υ -yields, high- p_T J/ Ψ and the high-mass part of the dilepton continuum as well as dijets with an L1-trigger. By design the momentum resolution is anticipated to be better than 4.7% depending on multiplicity. The pion rejection should be about a factor of 100 for momenta above 1 GeV/c in high multiplicity Pb-Pb collisions. The granularity is chosen appropriate to handle highest multiplicity events with an occupancy of about 34%. The massive

amount of readout electronics needed to achieve this granularity causes a lot of heat dissipation. As a result the electronics is water cooled, but to further minimize the power consumption the electronics is partially suspended to stand-by mode while no event has to be measured. Hence there is a necessity to wake them up, in order to take data when an interesting event occurs. To meet the timing requirements, a special wake-up signal generated by the TRD pre-trigger system is needed as described in chapter 4.1

Time-of-Flight Detector

The Time-of-Flight Detector (TOF) is made of multi-gap resistive-plate chambers (MRPCs) also covering a pseudo-rapidity range of about $|\eta| < 0.9$. It is used for particle identification in a momentum range up to 2.5 GeV/c for pions and kaons and 4 GeV/c for protons. It is designed to deal with a charged-particle density of $dN_{ch}/d\eta = 8000$ in Pb-Pb central collisions at an occupancy of less than 15%. TOF can achieve an intrinsic time resolution better than 40 ps and an efficiency close to 100%.

The device is placed between radii of 3.7 m and 3.99 m and forms a cylindrical shell around the TRD. It is divided into 18 sectors in ϕ and has a 5-fold segmentation in z direction. The whole detector is assembled from 10-gap double-stack MRPC strips (122 cm \times 13 cm) with 48 readout pads each placed in gas tight modules.

In addition to the detectors described above, there exists a High-Momentum Particle Identification Detector (HMPID), a PHOTon Spectrometer (PHOS) and an electromagnetic calorimeter (EMCal) and the ALICE COsmic Ray DETector (ACCORDE) all partially covering the central barrel.

3.2. Forward Detectors

Forward Multiplicity Detector

The Forward Multiplicity Detector FMD, a silicon strip detector, provides a charged particle multiplicity information in the pseudo-rapidity range of $-3.4 < \eta < -1.7$ and $1.7 < \eta < 5.0$. It is designed to handle high charged particle densities in central Pb-Pb collisions. Even in events with $dN_{ch}/d\eta = 8000$ one charged particle would occupy one strip on average.

T0 Detector

This detector is designed to deal with the following tasks:

- Generating a start time (T0) for the TOF, with a precision of about 50 ps
- Measuring the vertex position with a precision of ± 1.5 cm and providing an L0 trigger when the position is within the preset values
- Generating an early 'wake-up' signal for the TRD, prior to L0

Due to these tasks all signals have to be processed online to stay in time and the dead time of the detector should be less than the bunch-crossing period in pp collision (25 ns).

The detector is made of 24 Cherenkov counters in two arrays. T0-C is placed about 73 cm away from the Interaction Point (IP) at the C side and T0-A about 375 cm away from the IP at the A side, covering a pseudo-rapidity range of $-3.28 \leq \eta \leq -2.97$ and $4.61 \leq \eta \leq 4.92$, respectively. Due to these different positions the signals have to be aligned in the TRD pre-trigger system to achieve coincidence.

V0 Detector

The V0 detector also provides minimum-bias triggers for the central barrel detectors in pp and Pb-Pb collisions and participates in the measurement of luminosity in pp collisions. It consists of two arrays of scintillator counters named V0-A and V0-C. These arrays are assembled from four rings of eight scintillators each, covering a pseudo-rapidity range of $-3.7 < \eta < -1.7$ and $2.8 < \eta < 5.1$. The pseudo-rapidity coverage of the rings is shown in detail in table 3.1.

Ring	V0A	V0C
	η_{max}/η_{min}	η_{max}/η_{min}
0	5.1/4.5	-3.7/ - 3.2
1	4.5/3.9	-3.2/ - 2.7
2	3.9/3.4	-2.7/ - 2.2
3	3.4/2.8	-2.2/ - 1.7

Table 3.1.: Pseudo-rapidity acceptance of the V0 rings

Zero-Degree Calorimeter

The Zero-Degree Calorimeter (ZDC) is mainly designed to measure the centrality of a Pb-Pb collision. Therefore it measures the spectator nucleons and can provide this information as Level 1 Trigger (L1).

The ZDCs are located at 116 m on either side of the IP. Because of the fact that spectating protons and neutrons are separated by the magnets in the LHC beam line, ZDC is separated into two detectors: ZN for neutrons ($|\eta| > 8.7$) and ZP for protons with acceptance depending on the beam energy. Since some particles stay in the beam pipe and are not measurable by the ZDC, there is an electromagnetic calorimeter ZEM measuring the energy of particles emitted at forward rapidity ($4.8 < \eta < 6.7$) because the energy deposit there increases with the centrality of a Pb-Pb collision.

In addition to the detectors mentioned above there is the Photon Multiplicity Detector (PMD) in the forward pseudo-rapidity region of $2.3 \leq \eta \leq 3.7$ and a muon spectrometer (MUON) placed at $-4.0 < \eta < -2.5$ designed to measure heavy-quark vector-meson resonances in the $\mu^+\mu^-$ decay channel, which are not of particular interest in this thesis.

Not yet in place but already constructed are two new detectors increasing the coverage in the forward region. The ALICE Diffractive Detector (ADD1) covering

$-5.5 < \eta < -6.5$ is positioned behind the last muon absorber and the ALICE Diffractive A-side detector (ADA1) covering $5.5 < \eta < 6.5$ is supposed to find place at a distance of about 17 m and 20 m, respectively, from the interaction point. Both of them are scintillation detectors. In a second stage ADD2 and ADA2, which are two detectors at a distance of 55 m from the interaction point, are planned.

3.3. Trigger System

Due to the large interaction rate at LHC design luminosities an online selection of interesting events is needed to meet the Data Acquisition system (DAQ) bandwidth. This task is executed by the Central Trigger Processor (CTP). In order to achieve the fastest possible trigger response after an interaction, the trigger is divided into three levels. The first Level 0 (L0) is sent within $1.2 \mu\text{s}$ after the interaction. On account for this a L0 contribution must arrive at the CTP within a time window of 800 ns. This signal is early enough to start the readout of the non-pipelined electronics of some detectors. Fast trigger signals, which cannot arrive within in the window of L0, are included in Level 1 (L1), these trigger signals are sent within $6.5 \mu\text{s}$. Level 2 (L2) includes a past-future protection. This assures that no other events making the reconstruction of a highest multiplicity Pb-Pb collisions impossible occur during the detection time. Hence the L2 trigger, which is the final trigger signal, is sent after a protection interval of $88 \mu\text{s}$.

Further selection of the events is done by the High-Level Trigger (HLT) to reduce the data rate for all detectors, easily reaching 25 GB/s after trigger selection for Pb-Pb collisions, to a data rate of about 1 GB/s which can be archived by the DAQ.

3.4. Acceptance in Pseudo-Rapidity

The ALICE detectors cover combined a wide pseudo-rapidity range. In figure 3.1 an overview including the two detectors under construction ADD and ADA is given. T0 is not shown here because it covers only small fractions of the range covered by V0. The different trigger signals are available during different time intervals after a collision. While T0, TOF and V0 are available in time for a dedicated diffractive-gap trigger signal generated by the TRD pre-trigger system, the other ones are only available in higher trigger levels.

3.5. ALICE Studies on Central Diffraction

ALICE is not the only experiment planning to study diffraction at the LHC, but it has some advantages for central diffractive data taking. In comparison to the other large experiments at the LHC, it is able to measure tracks with lower p_T . The p_T acceptance in correlation with the pseudo-rapidity of the central barrels of the experiments is shown in figure 3.2. The precise p_T measurement is needed to determine the invariant mass of a centrally produced system. Furthermore the TRD Pre-Trigger System can be used to derive a L0 trigger signal dedicated to diffraction based on data from T0, V0 and TOF.

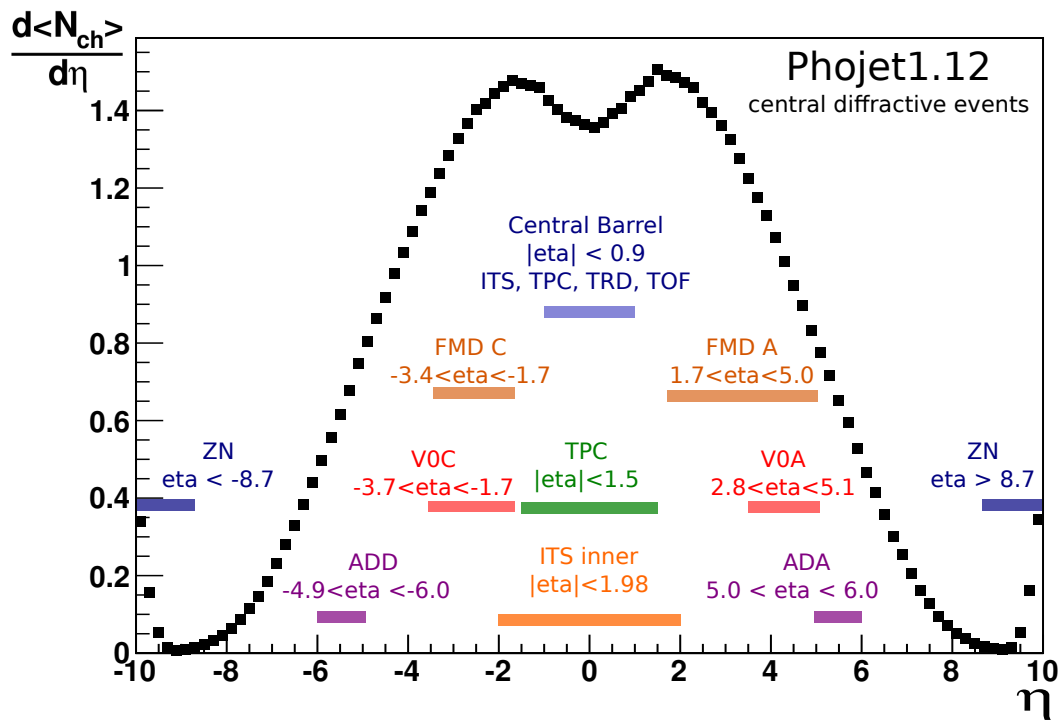


Figure 3.1.: Phojct1.12 [18,19] central diffractive event and ALICE pseudo-rapidity acceptance for different detectors

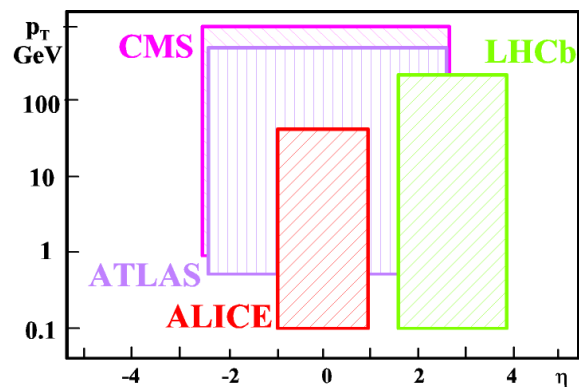


Figure 3.2.: Comparison of the $\eta - p_T$ acceptance of the experiments at LHC, taken from [20]

4. TRD Pre-Trigger Simulation Environment

4.1. TRD Pre-Trigger System Overview

In this chapter the principle behavior and design of the pre-trigger system is introduced. The 'L0 accept' signal issued by the CTP is distributed to the different detector systems and arrives approximately $1.2 \mu\text{s}$ after the interaction. This is too late to fulfill the requirements of a wake-up signal for the TRD which are described in chap. 3.1. The pre-trigger system produces a signal which is in time to wake up the TRD early enough. This is realized by generating the trigger signal inside L3 magnet. Together with the common ALICE trigger signals this signal is sent to the TRD supermodules.

To achieve a very fast signal generation only the following fast detectors are taken into account in the generation process:

- V0, described in chap. 3.2
- T0, described in chap. 3.2
- TOF, described in chap. 3.1

The final pre-trigger signal is generated in three stages containing Look Up Tables (LUTs) and a special case, the TLMU without LUT usage:

In the first stage, the analog signals coming from the T0 and V0 Photomultiplier Tubes (PMTs) are digitized and processed in the Front-End Boxes (FEBs). First the signals are amplified and split up. While a five-times amplified signal is used by the Front-End Electronics (FEE) of the TRD, the other ones are used by V0 and T0, respectively. FEE uses a comparator to convert the analog input signals to digital boolean values. These boolean values are combined to bit-vectors which then are processed by the first group of LUTs. This work is distributed to five electronic boards per side, one handling the 12 signals by T0 and four of them handling 8 signals by V0 each. Every board contains two LUTs.

In the second stage, the results produced by the LUTs of the first stage are combined and processed by the second group of LUTs. This is done by Control Box A (CB-A) on A side and Control Box C (CB-C) on C side with two LUTs each.

The special case is the TOF Logic Multiplicity Unit (TLMU). Here no processing with the help of LUTs is possible due to the number of input signals (576 TOF-

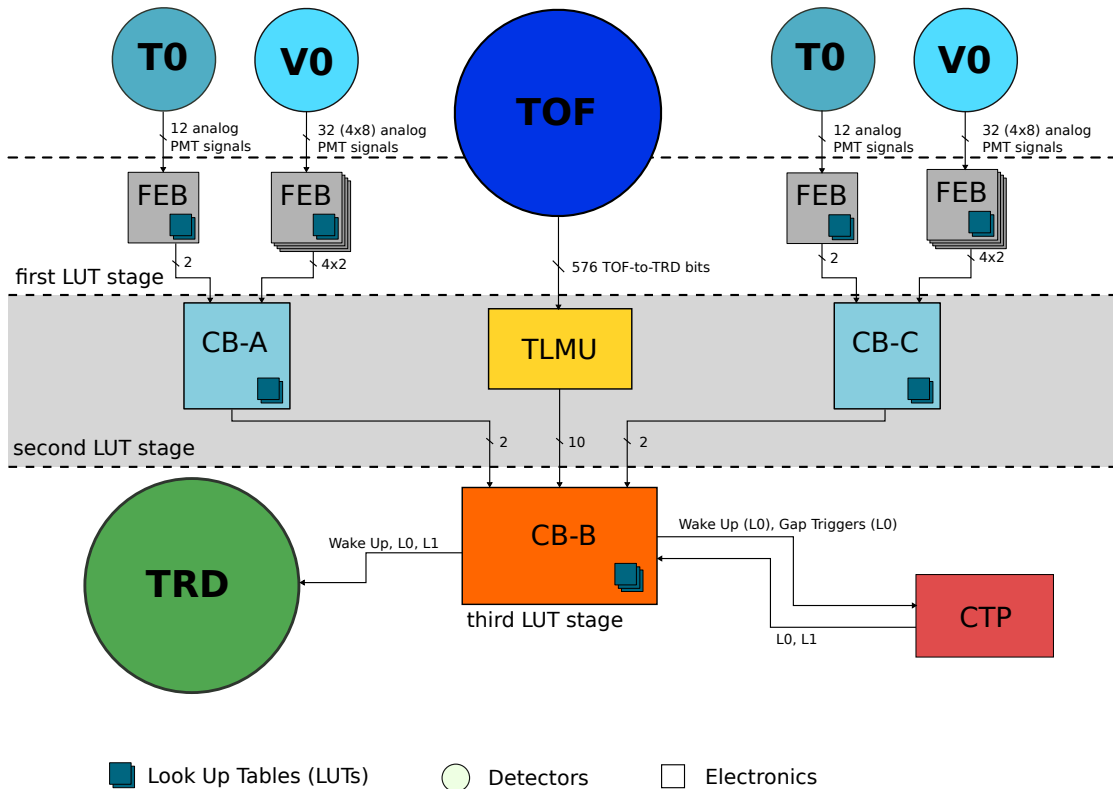


Figure 4.1.: Schematic diagram of the TRD Pre-Trigger System

to-TRD-bits) from TOF. Therefore in this unit a Field-Programmable Gate Array (FPGA) processes the input signals with two special functions:

- *Coincidence matrices*

There are three matrices to express coincidence between the 18 supermodules of TOF. 32 signals belonging to one sector of TOF are combined by logical OR. So it is, e. g., possible to use a matrix each to check whether there is coincidence in opposing TOF sectors (so-called back-to-back events) and also opposing TOF sectors and their nearest or the second nearest neighbor on one side (back-to-back ± 1 , back-to-back ± 2). With this function it is possible to identify particles which are emitted about back-to-back from the primary vertex.

- *Multiplicity slices*

This function allows the classification of the multiplicity seen by TOF in up to 9 ranges. The ranges are specified by a lower and an upper bound and can overlap for as much flexibility as possible.

In addition it is possible to configure which results of these functions should be available as output signals. A maximum of eight independent results can be selected.

In a third stage the results of the second stage and the results generated by the TLMU are combined and processed by two more LUTs. This stage is implemented

in the Control Box Bottom (CB-B). Here the actual pre-trigger signal is generated. The pre-trigger signal can be a combination of the output of the LUTs of CB-A and CB-C, the LUTs of the current stage, the TLMU output signals and also some testing inputs. Furthermore, in the future, special gap trigger signals for diffractive data acquisition will be generated here.

4.2. Software Description

In this chapter the design and functionality of the TRD Pre-Trigger Simulation Environment is described. The simulation is designed under the object oriented paradigm and the assumption to stay as close as possible to the hardware structure of the TRD Pre-Trigger System. Hence almost every significant piece of hardware is represented by a counterpart in software.

4.2.1. AliRoot

AliRoot is the ALICE offline framework for simulation. It is built upon the basis ROOT [21]. Except for large existing libraries, such as GEANT and some Monte Carlo event generators like Pythia6 [22] or Phojet [18, 19], this framework is based on the Object-Oriented programming paradigm and it is written in C++. AliRoot is capable to run in a cluster/cloud computing environment with Alice Environment (AliEn) [23], a lightweight grid framework and ALICE's key to the Worldwide LHC Computing Grid (LCG) [24]. The overall AliRoot layout is dis-

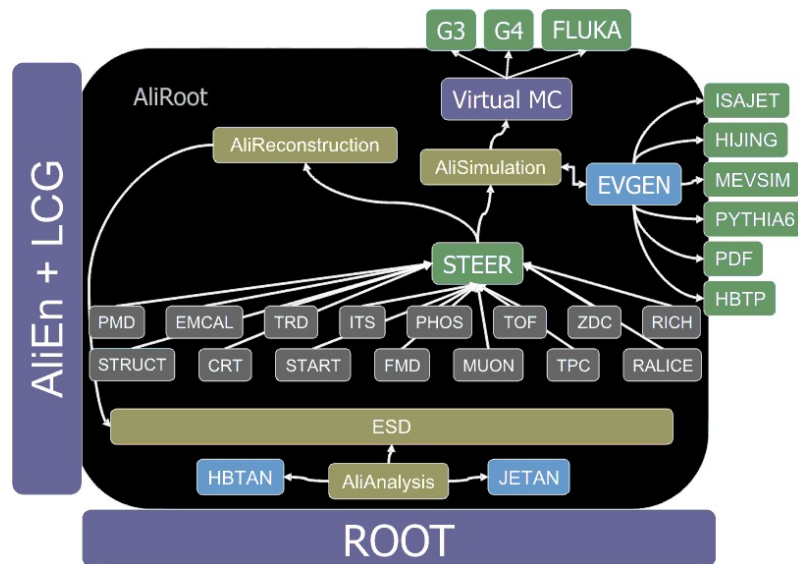


Figure 4.2.: AliRoot Layout, modified, taken from [25]

played in figure 4.2. The basis ROOT is shown below and AliEn + LCG on the left hand-side of AliRoot (black box). All AliRoot modules are centralized around the STEER (green box in the center). The detector modules are drawn with a gray box. The transportation frame works are shown on top of AliRoot (G3 for GEANT 3.21, G4 for GEANT4 and FLUKA). They are linked to Virtual MC which is ROOT's

interface for different geometry transport and detector response definitions. A selection of the possible event generators is shown on the right hand-side of the detector. They are integrated via the EVGEN module of AliRoot. The simulation process is steered by the class AliSimulation. All remaining classes belong to either the reconstruction or analysis part of AliRoot which are not considered in this thesis.

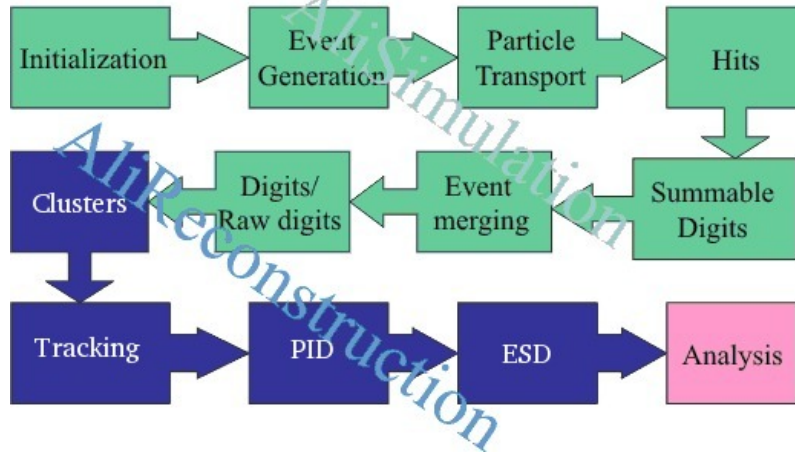


Figure 4.3.: AliRoot Execution Flow, simulation part in green, reconstruction in blue, taken from [25]

The TRD Pre-Trigger Environment is positioned at the end of the AliSimulation part (green boxes) of the processing chain. The pre-trigger simulation gains its results on the basis of digits.

4.2.2. Class to Hardware Component Assignment

All classes with a name containing “TRD”, apart from AliTRDTriggerL0 which was only modified, were implemented during this bachelor thesis.

4.2.3. Class Descriptions

Due to the naming conventions in AliRoot, the ALICE offline environment, every class of the simulation source code starts with “AliTRDptrg” to indicate that this class belongs to the TRD code (“TRD”) and especially the Pre-Trigger (“ptrg”). All configuration parameters are stored in an AliTRDptrgParam singleton class which is described below. In addition every class can be run with standard parameters and without an assigned configuration object.

AliTRDptrgLUT

This class provides basic LUT functionality. The implementation is done with integer arrays containing the result value. The input value is used as index for the look-up in the table and has to be a non-negative integer value and due to that fact the LUT size is limited to 31 input bits and 2^{31} table entries. The configuration can be done via a pointer to an existing array or by copying an

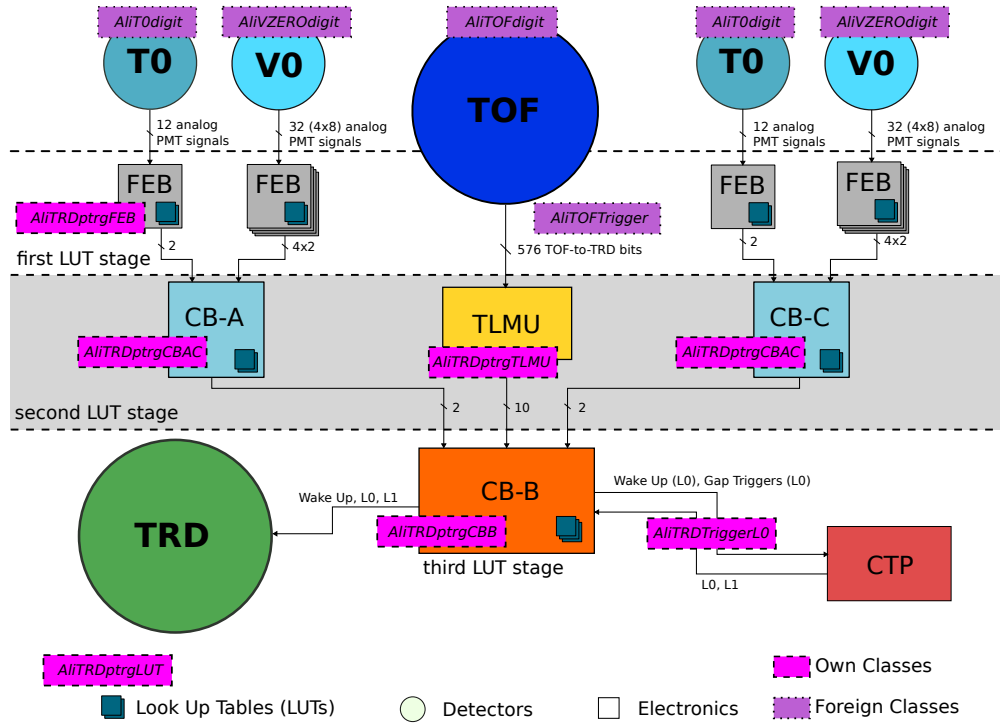


Figure 4.4.: Schematic diagram of the TRD pre-trigger system with the software classes corresponding to the hardware components

existing array.

The LUT-class is used in the FEBs and control boxes CB-A, CB-C and CB-B.

AliTRDptrgFEB

AliTRDptrgFEB acquires the analog signals from the corresponding V0 and T0 channels and processes them.

Incoming analog signals provided by AliT0digit and AliVZEROdigit are selected upon their channel and board number in case of V0. When configured for T0, 12 input channels are handled, in V0-mode 8. After selection the signals are discriminated with a threshold to suppress noise. Afterwards a bit vector containing the discriminated input signals is created and looked up in two LUTs to generate two independent output signals. These output signals are then processed in CB-A and CB-C. The digitizers producing the digits of V0 and T0 are adjusted to the behavior of detector's own hardware but the pre-trigger uses its own independent hardware for digitization. This difference in the signal processing chain complicates the usage of the same threshold parameters in simulation and online. As can be seen by the finite width of the pedestal in the V0 plot of figure 4.5, only V0 simulates noise behavior, T0 does not. A similar analysis should be considered for the online system. This has to be done via comparison of the pre-trigger results and T0 or V0 results. A direct comparison of the output from the hardware of detectors and the values generated by FEBs is impossible, because the values in the FEBs are not read out as of now. After each major source code change in T0's or V0's digitizers,

the pedestals should be analyzed, too.

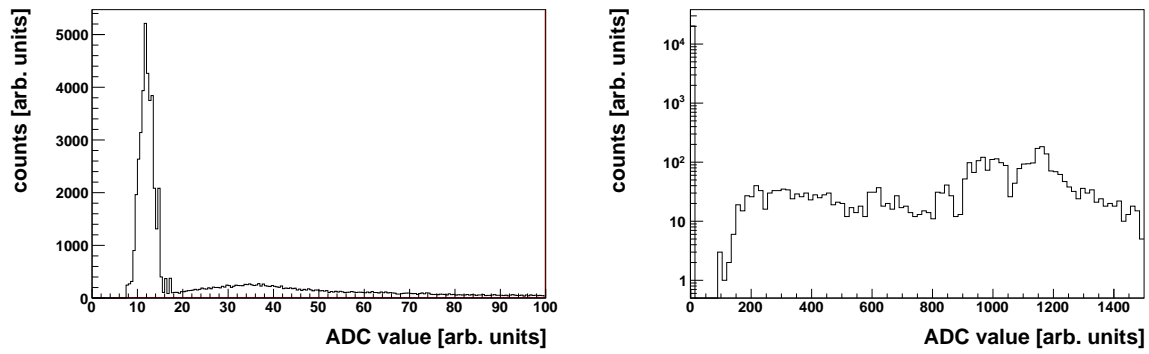


Figure 4.5.: Pedestal Plots of V0 (left) and T0 (right)

AliTRDptrgCBAC

This class is the implementation of CB-A and CB-C. These two instances have in principle the same functionality and therefore they are implemented in the same class and only differ in some configuration parameters at runtime. Each control box handles five FEBs, one acquiring V0 and four acquiring T0 signals. Their output signals are combined to another bit-vector which is also processed by two LUTs which are provided as output of the control box.

AliTRDptrgTLMU

The `AliTRDptrgTLMU` class is the direct counterpart of the hardware TLMU. The input signals read from `AliTOFdigits` are assembled to a boolean map of 18×32 bits (the so-called TOF-to-TRD-bits) by `AliTOFTrigger`. This boolean map is then converted to 18 bit-vectors containing 32 bits each (18 unsigned integer values) for faster processing with logical operations. The first operation is masking out noise bits with an input mask. Then the multiplicity in each bit-vector is counted and summed up at the end to define the overall multiplicity. This value is then compared to the upper and lower bounds of the multiplicity slices in order to gain the results. Then an activity bit-vector is generated which contains an active bit for each TOF sector with a multiplicity higher than zero. In order to process the coincidence matrices this vector will be combined with each matrix column. If the multiplicity of the result of the logical AND operation is greater or equal two, at least two of the sectors selected in the matrix vector and are active both in the activity vector and then coincidence matrix column and so the coincidence condition will be fulfilled. Although it is possible to generate a maximum of eleven output values only eight can be transmitted to the CB-B and so these eight ones can be selected with configuration parameters. Due to the configurability of the output signals some of the evaluation steps will be omitted if they are not needed to obtain the selected output.

AliTRDptrgCBB

`AliTRDptrgCBB` is the part of the software which combines the signals from the forward detectors at A and C side (V0 and T0) already combined by CB-A and CB-C and also from the central barrel from TOF preprocessed by the TLMU in a bit vector. This vector here is processed by three not only two LUTs. This is owed to the fact, that the pre-trigger should be used as diffractive-gap trigger as described in chapter 5.3 with three output signals which are directly taken from the outputs of LUTs. The pre-trigger wake-up signal can be assembled by the same variety as in the hardware (CB-A/C LUT outputs, CB-B LUT outputs, TLMU outputs), except of the testing signals.

AliTRDptrgParam

This is the class providing the configuration parameters for the other pre-trigger classes. It is a singleton class that is a class of which only one object is instanced by a whole application. This class contains a standard configuration making the simulation code capable of generating a valid TRD wake-up call and also valid gap trigger signals as defined in chap.5.3. Different configuration parameters can be loaded from configuration files (described in 4.3). The

`AliTRDptrgParam` interprets only known and needed parameters in the configuration file. All other parameters are omitted. The logical equations used in the configuration files to describe the behavior of LUTs are also processed in objects of this class. Because of the fact that the processing of the configuration is very complicated, this should be done only once in a simulation process and the configuration object should be kept as long as possible. All data tables and parameters are readable from outside via getter-functions. Therefore this class can be used to provide the configuration file processing to other programs written in C++. This is needed to use the same code also in the Detector Control System (DCS) which is an easy way to achieve a consistent behavior in simulation and online trigger configuration.

`AliTRDTriggerL0`

`AliTRDTriggerL0` connects the pre-trigger to the CTP. Hence it assigns the corresponding trigger signals of the CTP and then sets them active if a trigger occurs. Currently the following trigger signals are assigned:

- OHWU: pre-trigger wake-up signal
- OHSB: diffractive single-gap trigger
- OHDG: diffractive double-gap trigger

In the future it will perhaps be of interest to split the single gap trigger signal up into two signals (Side A, Side C). Due to the fact, that this class is instanced for every simulated event it uses an `AliTRDptrgParam`-object with a standard configuration to avoid the need for processing a configuration file every time an event is simulated.

4.3. Configuration Files

The configuration file as described in Appendix B plays an important role in the usage and also the usability of the pre-trigger. It is based on a concept proposed in a pre-trigger meeting and should be used for simulation and in the DCS to store run configurations.

Due to that fact there are parameters only used in online pre-trigger configuration. These parameters which are set by the corresponding PVSS tag editor panel [26] are omitted by the simulation code. They are used to store the `TAG`, `REVISION`, `TIMESTAMP/CREATION`, `TIMESTAMP/LASTUPDATE` and a `COMMENT`. Comments are allowed everywhere in the file with a '#' in front of the line. All configuration parameters corresponding to a certain part of the pre-trigger start with the associated name (TLMU, FEB, CBA, CBC, CBB).

The TLMU input mask `TLMU/IMASKSECxx` (`xx` determines the TOF sector) is assigned as binary number for each of the 18 sectors (0 to 17). The `TLMU/STRETCH` is only of interest in the hardware. A coincidence matrix can consist of a maximum of 18 entries (vectors of 18 bits) `TLMU/CMATRIXx/SECxx`. Each entry should contain at least two active bits ('1') to describe a coincidence of two sectors. It is possible to define up to three coincidence matrices. The nine multiplicity slices are defined by `TLMU/MCNTRx/THR min max`. The condition is evaluated according to the equation

$min < multiplicity \leq max$. Due to the difference between the number of possible evaluations and output signals, they are defined by TLMU/OUTMUX $\langle x \rangle \langle x \rangle$ with up to eight parameters. Possible parameters are CM0 to CM2 to use the coincidence matrices, MC0 to MC8 for multiplicity slices and SEQ0 to SEQ4 to select the trigger sequence which is not of interest in the simulation.

For each of the FEBs, the digitization threshold for the analog values from the PMTs and the delay and the multiplicity condition of the LUTs can be configured. The identifiers are summarized in table 4.1. Values are separated from each other and the identifiers with blanks or tabs. The multiplicity conditions of the LUTs are formed like M(input bit mask)>multiplicity. The delay parameter is not of interest here.

Parameter	Detector	Side	Identifiers	Values	Variables
digitization thresholds	T0	A	FEB/T0/A/THR	12 integers	
		C	FEB/T0/C/THR	12 integers	
	V0	A	FEB/V0/Ax/THR	8 integers	$x \in \{0, 1, 2, 3\}$
		C	FEB/V0/Cx/THR	8 integers	$x \in \{0, 1, 2, 3\}$
delay	T0	A	FEB/T0/A/DELAY	12 integers	
		C	FEB/T0/C/DELAY	12 integers	
	V0	A	FEB/V0/Ax/DELAY	8 integers	$x \in \{0, 1, 2, 3\}$
		C	FEB/V0/Cx/DELAY	8 integers	$x \in \{0, 1, 2, 3\}$
multiplicity	T0	A	FEB/T0/A/LUT/y	see text	$y \in \{0, 1\}$
		C	FEB/T0/C/LUT/y	see text	$y \in \{0, 1\}$
	V0	A	FEB/V0/Ax/LUT/y	see text	$x \in \{0, 1, 2, 3\}$, $y \in \{0, 1\}$
		C	FEB/V0/Cx/LUT/y	see text	$x \in \{0, 1, 2, 3\}$, $y \in \{0, 1\}$

Table 4.1.: Parameters for FEB configuration

For the control boxes A and C there are only two LUTs each to be configured. But these are configured with the help of logical equations. Each FEB output signal has its own identifier: T0_0 for T0 LUT 0, T0_1 for LUT 1. The signals from V0's FEBs need another suffix to identify the board: V0-0_0 is LUT output 0 from board 0 and V0-2_1 means board 2 and LUT 1. A signal can be negated by a '!' in front of the identifier. As logical operators || (OR) and && (AND) are allowed. AND is always evaluated before OR. In addition to that it is possible to use brackets in order to define subterms.

The LUTs of the CB-B are configured in the same way as the ones of the other two Control Boxes (CBs). Identifiers named TLMU_0 to TLMU_7 specify the output signals

of the TLMU. The outputs of CB-A are named `CB-A_0` and `CB-A_1` and the ones of CB-C analogously `CB-C_0` and `CB-C_1`. Furthermore there are a lot of parameters which are only used by the detector hardware and not by the simulation and will not be described here. A description of all parameters and corresponding registers of the CB-B can be found in the TRD Documentation Project [27].

5. Diffractive-Gap Trigger Evaluation

In this chapter the possible use of the TRD pre-trigger as an L0 trigger for central diffractive events is scrutinized. The following evaluations have been done with AliRoot trunk revision 40890 and patches 41318 as well as 41319, GEANT3 and ROOT revision 33337 trunk.

This evaluation is based on proton-proton collisions with a maximum luminosity of $L = 5 \cdot 10^{30} \text{ cm}^{-2}\text{s}^{-1}$. This maximum is defined by the TPC and is used for all further evaluations.

All plots shown in this chapter are based on the physical primary particles, particles produced in the collision including products of strong and electromagnetic decays and excluding feed-down from weak decays of strange particles, produced by the corresponding Monte Carlo generator.

Lead-lead collisions are not considered in this thesis.

5.1. Monte Carlo Event Generator Selection

Since Pythia6 and Pythia8 do not contain central diffraction, two separate event generators were used [22, 28].

The minimum bias events, for simulating the background, were generated by Pythia8. This version of Pythia was chosen, since it has an improved implementation of diffractive dissociation processes as compared to Pythia6. The diffractive dissociation processes are very important because their pseudo-rapidity distribution signature is assumed to cause most of the false trigger events.

The simulation of central diffractive ones turned out to be quite a challenge as most of the generators, dedicated to these events, do not provide an interface to ROOT or even AliRoot. Furthermore, most of them are specialized to specific tasks or models. Phojet was the only one with an interface to AliRoot, which is provided through the DPMJet event generator and its interface to the EVGEN module of AliRoot [18, 19]. DPMJet allows access to the Phojet configuration and so central diffractive events can be selected for generation. Unfortunately, the development of Phojet ended in the year 2003 and so this generator does not take into account the progress of theoretical understanding in the last few years. Another generator that will implement central diffraction in the future is HERWIG++, but is not ready yet.

As shown in figure 5.1 the events show up with different pseudo-rapidity signatures. While the minimum bias events without diffractive processes have the highest multiplicity of charged particles per unit of pseudo-rapidity, the diffractive dissociation part has much smaller values of multiplicity. This results in a somewhat lower dis-

tribution for the overall minimum bias events including diffractive dissociation. The central diffractive events have the lowest multiplicity of charged particles per unit of pseudo-rapidity.

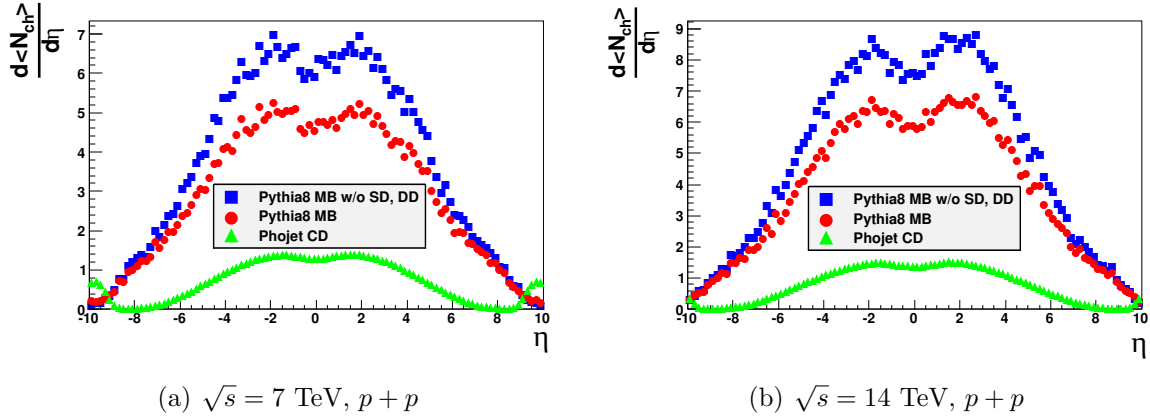


Figure 5.1.: Pseudo-rapidity distributions of charged particles

While the minimum bias events have an average multiplicity of about 62 charged particles, the minimum bias events excluding the diffractive dissociation events have a mean multiplicity of about 78. The central diffractive events have an average multiplicity of about 17 charged particles per event. This fits well to the pseudo-rapidity distributions in figure 5.1, showing the pseudo-rapidity distributions of charged particles for an average event generated by Pythia8 with standard minimum bias settings including diffractive dissociation (red markers) and without diffractive dissociation (SD/DD) (blue markers) as well as Phojet with central diffractive settings (green markers).

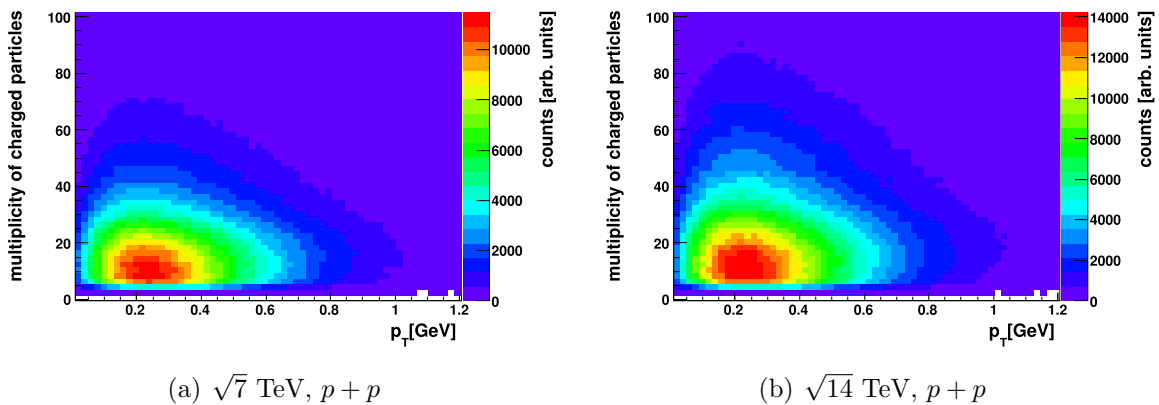


Figure 5.2.: $p_T - N_{ch}$ -correlation for central diffractive events generated by Phojet

As shown in figure 5.2 for the Phojet events, no correlation between p_T and N_{ch} is seen. It is clearly visible, that the tracks of the central diffractive events are of low multiplicity and low p_T .

5.2. Diffractive Cross Sections

	GLMM		KMR		Pythia 8.130		Phojet 1.12	
	7 TeV	14 TeV	7 TeV	14 TeV	7 TeV	14 TeV	7 TeV	14 TeV
σ_{tot} (mb)	81.3	92.1	80.0	88.0				
σ_{bg} (mb)					71.4	79.3		
σ_{el} (mb)	18.3	20.9	18.0	20.1				
σ_{sd} (mb)	10.7	11.8	11.8	13.3	13.7	14.4		
low M (mb)	9.4	10.5	4.7	5.1				
high M (mb)	1.2	1.3	7.2	8.2				
σ_{dd} (mb)	5.7	6.1	9.8	13.4	9.3	10.3		
σ_{mb} (mb)					48.5	54.7		
σ_{cd} (mb)							1.3	1.4

Table 5.1.: Cross sections at $\sqrt{s} = 7$ TeV and $\sqrt{s} = 14$ TeV, see text for description

The table 5.1 displays the cross sections of Pythia8.130 which are comparable with the ones of GLMM (E. Gotsman, E. Levin, U. Maor and J.S. Miller) and KMR (M.G. Ryskin, A.D. Martin and V.A. Khoze) [28–30]. None of these cross sections has been measured yet. Only the values for 14 TeV have been published, the values for 7 TeV shown in table 5.1 have therefore been calculated by a linear extrapolation to the Tevatron cross sections at $\sqrt{s} = 1.8$ TeV and LHC’s maximum energy $\sqrt{s} = 14$ TeV [29–31]. This approximation is dominated by the uncertainties and differences of the predictions. The cross sections of Pythia8 and Phojet 1.12 are taken from the generator log files created during the evaluation process [18, 19].

5.3. Definition of a Gap Trigger

The diffractive-gap triggers are defined as follows. In the central barrel there have to be at least two charged particles measured by TOF. The single gap A trigger additionally requires no hits of particles at V0 and T0 on A side. For a single gap C trigger, there must not be hits at C side. A double-gap trigger does not allow hits in V0 and T0 on A *and* C side.

Separate evaluations are done for “noise” at V0 at either one or both detectors. In the “noise” configurations the multiplicity at one of the V0 rings per side is allowed to be one. T0 is not allowed to have any signal for the definition of a gap at the corresponding side.

5.4. Trigger Evaluation Minimum Bias Events

The total cross section of the minimum bias events was about 71 mb at $\sqrt{s} = 7$ TeV and 79 mb at $\sqrt{s} = 14$ TeV. Together with the luminosity $L = 5 \times 10^{30} \text{ cm}^{-2}\text{s}^{-1}$ this

results in an event rate of about $3.59 \cdot 10^5 \text{ s}^{-1}$ and $3.95 \cdot 10^5 \text{ s}^{-1}$, respectively. An overall number of 262000 events at 7 TeV and 173000 events at 14 TeV was generated and evaluated. In order to determine the influence of diffractive dissociation processes on the background triggering rate, the minimum bias events have been evaluated again with a filter rejecting the diffractive dissociation events. These events are tagged with an event-type id during the generation process in Pythia8. The remaining minimum bias events are supposed to have a cross section of $\sigma = 49 \text{ mb}$ (7 TeV) and $\sigma = 55 \text{ mb}$ (14 TeV), which results in an event rate of about $R = 2.43 \cdot 10^5 \text{ s}^{-1}$ and $R = 2.74 \cdot 10^5 \text{ s}^{-1}$, respectively. The trigger rates corresponding to the minimum bias events with and without diffractive dissociation are listed in table 5.2 and table 5.3, respectively. The settings for the gap trigger were chosen according to the definition in subsection 5.3. The different configurations allowing noise at V0 did not result in higher triggering rates. This is an evidence that the noise rejection with the current set of thresholds works.

Trigger	Events	Fraction	Suppression	L0 Rate [Hz]
$\sqrt{s} = 7 \text{ TeV}$				
simulated / zero bias	262000			
single gap A	6869 ± 83	0.02622 ± 0.00032	38.14 ± 0.47	$(9.41 \pm 0.12) \times 10^3$
single gap C	6849 ± 83	0.02614 ± 0.00032	38.25 ± 0.47	$(9.38 \pm 0.12) \times 10^3$
double gap	274 ± 17	0.00105 ± 0.00006	956 ± 58	375 ± 23
$\sqrt{s} = 14 \text{ TeV}$				
simulated / zero bias	173000			
single gap A	6239 ± 79	0.03606 ± 0.00047	27.73 ± 0.36	$(14.26 \pm 0.19) \times 10^3$
single gap C	4462 ± 67	0.02579 ± 0.00039	38.77 ± 0.58	$(10.19 \pm 0.15) \times 10^3$
double gap	184 ± 14	0.00106 ± 0.00007	940 ± 70	419 ± 31

Table 5.2.: Trigger rates for Pythia minimum bias events including diffractive dissociation

The errors shown here are assumed to be mainly of statistical nature, the uncertainty of the cross section predictions and detector efficiencies are not taken into account. The double-gap trigger for the minimum bias events without diffractive dissociation has no event, therefore the suppression can be assumed to be on the order of 10^5 . It can be deduced, that a large fraction of triggers caused by background events, are due to the diffractive dissociation events. Despite the fact that about two thirds of the background cross section is caused by inelastic hadronic events and one third caused by diffractive dissociative events, the triggering rate decreases by a factor of 15 for events at $\sqrt{s} = 14 \text{ TeV}$ and 13 at A side and 22 at C side for a center-of-mass energy of $\sqrt{s} = 7 \text{ TeV}$. The large asymmetry is caused by the different range and positions of the V0-A and V0-C in pseudo-rapidity. This asymmetry loses importance at 7 TeV because the amount of particles at V0 decreases. In order to explain the asymmetries and the difference between the two center-of-

Trigger	Events	Fraction	Suppression	L0 Rate [Hz]
$\sqrt{s} = 7 \text{ TeV}$				
simulated / zero bias	179208			
single gap A	537 ± 23	0.00300 ± 0.00013	333 ± 14	729 ± 32
single gap C	320 ± 18	0.00179 ± 0.00010	560 ± 31	435 ± 24
double gap	2 ± 1.4	$(1.12 \pm 0.79) \times 10^{-5}$	$(9.0 \pm 6.3) \times 10^4$	2.8 ± 1.9
$\sqrt{s} = 14 \text{ TeV}$				
simulated / zero bias	120581			
single gap A	401 ± 20	$(3.33 \pm 0.17) \times 10^{-3}$	300 ± 15	912 ± 47
single gap C	298 ± 17	$(2.47 \pm 0.12) \times 10^{-3}$	405 ± 23	676 ± 33
double gap	0	?	?	?

Table 5.3.: Trigger rates for Pythia minimum bias events without diffractive dissociation

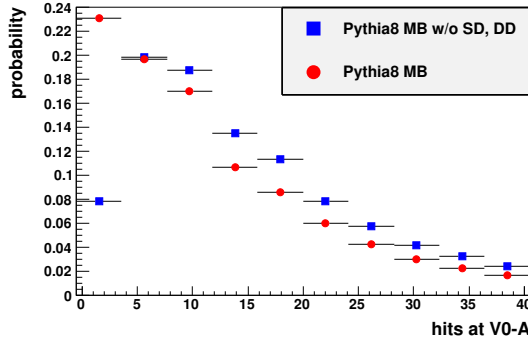


Figure 5.3.: Particles at V0 in an average minimum bias event

mass energies, it would be nice to fit a function to the particle distribution at V0. The multiplicity of hits at V0-A in an average minimum bias event is plotted in figure 5.3. Due to the huge influence of the diffractive dissociation processes in the minimum bias events and therefore a peak at zero particles, it is not possible to fit a distribution function here but only a convolution or superposition of one describing the inelastic hadronic events and one or even more describing the diffractive events. For the minimum bias events without diffractive dissociation the distribution of the particles is only caused by inelastic hadronic processes. In this case a fit should be easier to achieve. Several different fit functions, for example Poisson, Negative Binomial Distribution have been tried for fitting but have failed. The average number of particles hitting the whole detector and the detector on average per unit of pseudo-rapidity which is derived from a $dN_{ch}/d\eta$ plot, are summarized in table 5.4. When applying the gap triggers on minimum bias events, the pseudo-rapidity distribution changes. While the single-gap triggers select events with a single diffractive dissociation pseudo-rapidity signature, the double-gap trigger selects mainly double

\sqrt{s}	Event type	Particles at the whole detector		Particles per unit of η	
		$V0-A$	$V0-C$	$V0-A$	$V0-C$
7 TeV	min bias	9.5	10.4	4.1	5.2
	min bias w/o SD, DD	12.3	13.7	5.3	6.9
	central diffractive	2.3	2.7	1.0	1.3
14 TeV	min bias	12.6	13.4	5.5	6.7
	min bias w/o SD, DD	16.3	17.2	7.1	8.6
	central diffractive	2.6	3.0	1.1	1.4

Table 5.4.: Number of particles measured at V0 in an average event.

diffractive dissociation events. In figure 5.4 the distribution of charged particles for an average event (black squares), an average event generating single-gap trigger A (red circles), an average event generating single-gap trigger C (blue triangles) and an average event generating a double-gap trigger (green triangles) at the center-of-mass energies of 7 TeV and 14 TeV as well as with and without diffractive dissociation is shown. The distributions of charged particles for an average minimum bias event

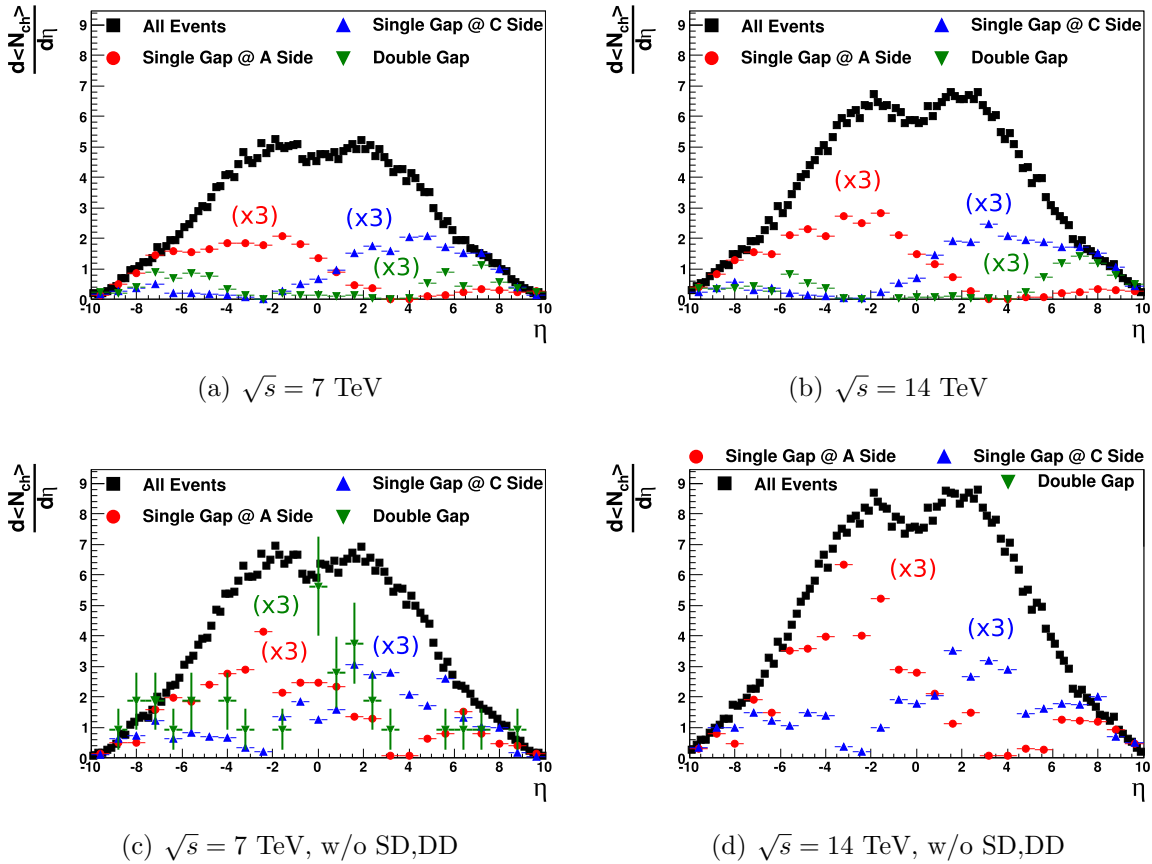


Figure 5.4.: Pseudo-rapidity distributions of charged particles for Pythia minimum bias events

excluding diffractive dissociation suffer from the low trigger rates for the single gap and double-gap triggers. In order to improve the statistic the gap trigger distributions have been rebinned and only the average of four bins is drawn. The apparent problem that particles are in the gap region can be explained by the fact, that the distribution is based on the event generator output and that possible decays and rescatterings are not taken into account. While single diffractive events, causing a single trigger, usually also produce few particles in the region of the central as visible in figure 5.4a or figure 5.4b, double diffractive events evidently causing the double-gap triggers by definition should have a large gap in the central pseudo-rapidity region. Because there is no noise implemented in the trigger simulation of TOF, there must be a physical explanation for these triggers, one of them is pair creation.

5.5. Trigger Evaluation Central Diffractive Events

According to Phojet's log files the cross sections for central diffractive events are $\sigma = 1.3 \text{ mb}$ at 7 TeV and $\sigma = 1.4 \text{ mb}$ at 14 TeV. At a luminosity $L = 5 \cdot 10^{30} \text{ cm}^{-2} \text{ s}^{-1}$ this results in event rates of $R = 6.5 \cdot 10^3 \text{ s}^{-1}$ and $R = 7 \cdot 10^3 \text{ s}^{-1}$, respectively. In total 277000 events at 7 TeV and 374000 at 14 TeV were generated and evaluated. The results are summarized in table 5.5. The additional configurations with noise, which is defined by additional single hits either at A or C side or even at both sides, did not influence the triggering rates either, because the proton remnants are not seen by V0 and since they are expected at absolute values of pseudo-rapidity larger than nine. This can be seen in figure 5.1.

\sqrt{s}	Trigger	Events	Efficiency	L0 Rate [Hz]
7 TeV	simulated / zero bias	277000		
	single gap A	33575 ± 183	0.12121 ± 0.00070	787 ± 5
	single gap C	26211 ± 162	0.09462 ± 0.00061	615 ± 4
	double gap	5391 ± 73	0.01946 ± 0.00027	126 ± 2
	14 TeV	simulated / zero bias	374000	
14 TeV	single gap A	42845 ± 207	0.11456 ± 0.00055	802 ± 4
	single gap C	35589 ± 189	0.09516 ± 0.00050	666 ± 4
	double gap	6134 ± 78	0.01640 ± 0.00021	115 ± 2

Table 5.5.: Trigger rates for Phojet central diffractive events

The asymmetric trigger rates already seen for the minimum bias events, are also visible for the central diffractive events, however they are not as pronounced as for the minimum bias events. This can be explained on the basis of the smaller amount of particles in a central diffractive event resulting also in a smaller absolute difference. The corresponding value can be found in table 5.4. Furthermore the trigger rates of the central diffractive events are not as strongly correlated with the center-of-mass energies as they are for the minimum bias events. This is a result of the almost

identical cross sections which differ by less than 10% and the marginal changes in the distribution of charged particles.

The average pseudo-rapidity signature of the central diffractive events is changed by the triggers as plotted in figure 5.5. All events generated by Phojet1.12 are drawn

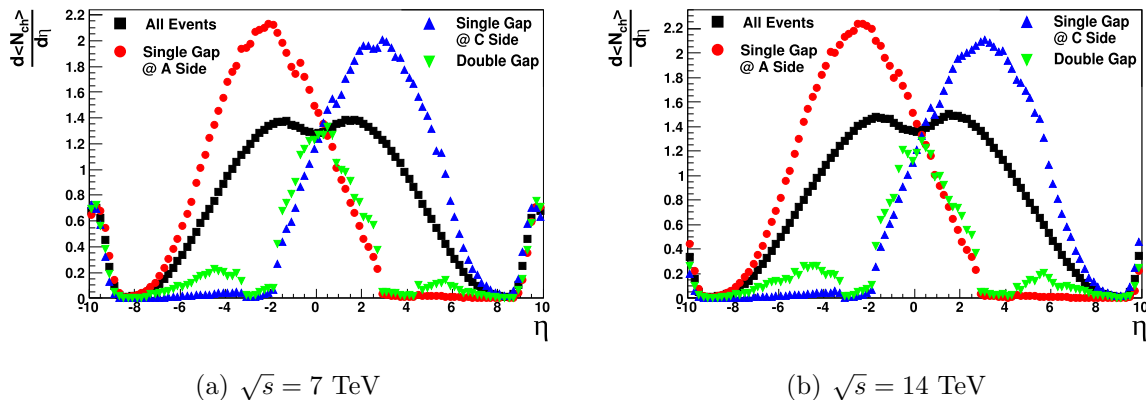


Figure 5.5.: Pseudo-rapidity distribution of charged particles for an average Phojet event

with black squares, the distribution corresponding to the events generating a single gap trigger at A side are drawn with red circles, the ones generating with a single-gap trigger at C side with blue triangles and those generating a double-gap trigger with green triangles. While the single gap triggers select the events which show a multiplicity distribution shifted slightly away from the corresponding gap side, the double gap trigger selects the events at central pseudo-rapidity. ALICE is able to measure in the central barrel in a pseudo-rapidity range of $|\eta| < 0.9$ up to $|\eta| < 1.5$, and so a criterion for a good measurement of the physical properties of a centrally produced system is the fraction of the events seen by the central detectors. This fraction was evaluated for multiplicity and invariant mass. The results are plotted in figure 5.6 for measurement ranges of $|\eta| < 0.9$, $|\eta| < 1.2$ and $|\eta| < 1.5$. In an ideal measurement all data points should be located on the diagonal, in a real one they should be located below. Otherwise the correlation is likely to be spoiled by pile-up events. In the figures an improvement for systems below $3 \text{ GeV}/c^2$ is clearly visible when the pseudo-rapidity range is changed from $|\eta| < 0.9$ to $|\eta| < 1.5$. For higher masses the statistic is low but, there also seems to be an improvement. For the multiplicity the measured fraction is also improved, but due to the discrete values the effect is not as clearly visible as for the invariant mass. However the extension of the measurement range is a trade-off between the measured fraction and the measurement precision, since all tracks in the region $|\eta| > 0.9$ are measured less precisely. An estimation of the fraction of the measured particles can be determined by multiplicity measured with the inner ITS layer and the FMD covering the range of $-3.4 < \eta < 5.0$. Most of the particles of the events selected by the double-gap trigger, designated by the green markers in figure 5.5 are distributed in this pseudo-rapidity region. In addition to the considerations above the detecting and reconstruction efficiency has to be taken into account.

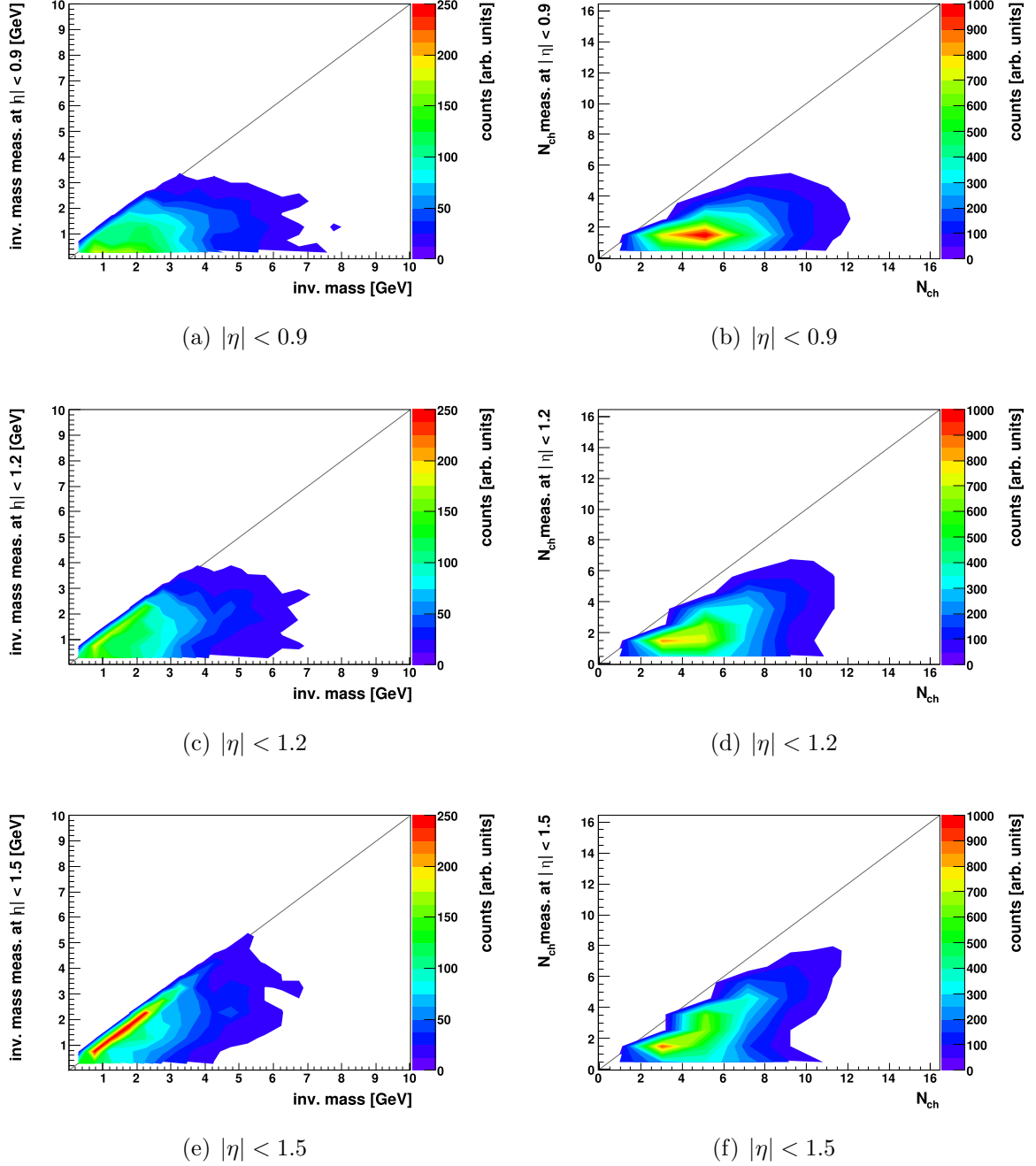


Figure 5.6.: Correlation of true and measured invariant mass (left) and correlation of true and measured multiplicity (right) in different pseudo-rapidity ranges.

5.6. Trigger Evaluation Summary

The trigger evaluation of central diffractive events and the corresponding background is summarized in table 5.6. For the luminosity a value of $L = 5 \times 10^{30} \text{ cm}^{-2}\text{s}^{-1}$ is used and the cross sections are taken from table 5.1. The single-gap triggers result

\sqrt{s}		single gap A	single gap C	double gap
7 TeV	Background (Pythia)	9410 s ⁻¹ (92.3%)	9380 s ⁻¹ (93.8%)	375 s ⁻¹ (74.9%)
	central diffractive events (Phojet)	787 s ⁻¹ (7.7%)	615 s ⁻¹ (6.2%)	126 s ⁻¹ (25.1%)
	total	10197 s ⁻¹	9995 s ⁻¹	501 s ⁻¹
14 TeV	Background (Pythia)	14260 s ⁻¹ (94.7%)	10190 s ⁻¹ (93.9%)	419 s ⁻¹ (78.5%)
	central diffractive events (Phojet)	802 s ⁻¹ (5.3%)	666 s ⁻¹ (6.1%)	115 s ⁻¹ (21.5%)
	total	15062 s ⁻¹	10856 s ⁻¹	534 s ⁻¹

Table 5.6.: L0 trigger rate summary

in very high total trigger rates on the order of 10 kHz. These rates are above the maximum TPC readout rate of 1400 Hz. As a result the single gap triggers only could be used at full rate without the TPC or up to an L2 rate of about 1400 Hz and disabled past-future protection. One possibility to reduce the trigger rate is a downscaling reading out only every tenth event or even less. This scaling can be done with a simple counter in the TRD pre-trigger system or in the CTP. An implementation in the pre-trigger would have the advantage, that for the discarded events no pre-trigger wake-up call is generated. The efficiency of this trigger signals is clearly below 10%.

At the energies of 7 TeV and 14 TeV the double gap trigger results in a total trigger rate of 501 Hz and 534 Hz, respectively. The corresponding efficiency is 25.1% and 21.5%, respectively. If the full DAQ bandwidth is available, it should be possible to process a very large fraction of the events at these rates.

At L0 level the CTP can require that for a gap trigger signal, the pixelmult2 trigger of the SPD is active, in order to cross check whether there is a centrally produced system. This procedure eliminates spurious L0 triggers generated in the TRD pre-trigger system based on noise in TOF. These rates have to be further processed by the HLT in order to reduce the data rate to a value that could be written to the storage by DAQ. One possibility to mask out triggers caused by noise in TOF is

the rejection of events which do not have at least two charged tracks in the central barrel measured by ITS or TPC. Furthermore the V0 and T0 contribution can be verified using FMD. A reduction of triggers caused by the diffractive dissociative events can be done with the help of ZDC, because for pure central diffractive events, without diffractive dissociation, nothing should be seen there. In addition to that we are looking for final states consisting of a certain number of charged particles, so we can discriminate the amount of events by a further multiplicity condition. This condition should not be chosen too tight, because additional charged particles can be produced by pair creation.

Noise has to be considered for the gap trigger approach. Noise in TOF can cause a false indication for the existence of a centrally produced system. The influence of noise at TOF can be reduced with the input masks in the TLMU and the use of the multiplicity trigger signal of the SPD at the CTP. If noise caused by V0 and T0 is not suppressed with the correct discrimination threshold, it can destroy the pseudo-rapidity gap. A technique to reduce that is to use a less tight gap condition and allow single hits at V0 and T0.

An additional trigger signal is only an advantage, when the fraction of desired events is increased by the usage of the new trigger signal. This is the case here, because the minimum bias trigger signals are mainly based on interactions seen by V0 and SPD's minimum bias signal. As we require pseudo-rapidity gaps at V0, the new trigger signals allow data taking of a new class of events, which are suppressed by the minimum bias trigger signals.

6. Summary and Outlook

The TRD pre-trigger system is now implemented in AliRoot including the full processing chain which is using V0, T0 and TOF as input signals. These signals are then processed in the two control boxes CB-A, CB-C and the TLMU for TOF. The final trigger decision is made by the CB-B, where all pre-results are combined. The behavior is exactly the same but there are some deviations from the actual hardware implementation due to use of digits for V0 and T0. With the correct selection of the input thresholds for V0 and T0, this difference in the processing chain can be minimized. The simulation already implements the pre-trigger configuration file, which in addition is foreseen to be used by the detector control system.

Based on the simulation environment of the TRD pre-trigger system developed within this thesis, an evaluation of a diffractive-gap trigger at L0 level was performed. The results indicate that the double-gap trigger can be used to select central diffractive events in proton-proton collisions at center-of-mass energies of 7 TeV and 14 TeV. Trigger rates are ~ 500 Hz with 25.1% efficiency at $\sqrt{s} = 7$ TeV and 534 Hz with 21.5% central diffractive events at $\sqrt{s} = 14$ TeV. Both rates are sufficiently below the maximum readout rate of the TPC of about 1400 Hz and therefore a parallel use with other interaction triggers without a scaling is possible. The single gap trigger causes very high rates and is therefore problematic, because the normal data taking with other interaction triggers can be disrupted by such high trigger rates. The single-gap trigger rate varies from slightly below 10 kHz at 7 TeV to about 15 kHz at 14 TeV at a luminosity $L = 5 \cdot 10^{30} \text{ cm}^{-2}\text{s}^{-1}$. Most of the background triggers are caused by diffractive dissociative events and not by inelastic hadronic events. The percentage of central-diffractive events causing a single-gap trigger varies from 5.3% to 7.3% and is significantly below the efficiency of the double-gap trigger. As the single-gap trigger is above the TPC readout rate, not all events causing a trigger can be read out. Such a trigger can, however, be downscaled in order to meet the available bandwidth of the DAQ.

Further studies on the efficiency of the pre-trigger system based on the available data from cosmic runs and the beam data taken at 7 TeV as well as a cross check with newer Monte Carlo generator tunes or even new generator implementations can be used to increase the validity of this evaluation. The main problem is the uncertainty about the cross sections and particle distributions as well as transverse momentum distributions at 7 TeV and also 14 TeV due to the fact that the analysis of the data taken recently is still in an early phase.

A. Acronyms and Technical Terms

ALICE	A Large Ion Collider Experiment
AliEn	Alice Environment
CERN	Conseil Européen pour la Recherche Nucléaire
CB	Control Box
CB-A	Control Box A
CB-B	Control Box Bottom
CB-C	Control Box C
CTP	Central Trigger Processor
DAQ	Data Acquisition system
DCS	Detector Control System
DD	Double Diffractive Dissociation
FEB	Front-End Box
FEE	Front-End Electronics
FMD	Forward Multiplicity Detector
FPGA	Field-Programmable Gate Array
HLT	High-Level Trigger
ISR	Intersecting Storage Rings
ITS	Inner Tracking System
IP	Interaction Point
LCG	Worldwide LHC Computing Grid
LHC	Large Hadron Collider
LUT	Look Up Table
PMT	Photomultiplier Tube
QCD	Quantum Chromodynamics
QGP	Quark-Gluon Plasma
SD	Single Diffractive Dissociation
SDD	Silicon Drift Detectors
SPD	Silicon Pixel Detectors
SSD	Silicon micro-Strip Detectors
TLMU	TOF Logic Multiplicity Unit
TOF	Time-of-Flight detector
TPC	Time-Projection Chamber
TRD	Transition Radiation Detector
ZDC	Zero-Degree Calorimeter

B. Pre-Trigger Configuration File

```
1 #
  # Pre-trigger run time parameter example file
3 # which should be generated by PVSS tag editor panels
  #
5
  # Configuration infos
7 TAG 120
  REVISION 123
9 TIMESTAMP/CREATION      YYYY-MM-DD hh:mm:ss
  TIMESTAMP/LASTUPDATE    YYYY-MM-DD hh:mm:ss
11 COMMENT example configuration (2010-03-31) changes according to PT
    meeting

13 # TLMU input masks
  TLMU/IMASK/SEC00      1111_1111_1111_1111_1111_1111_1111_1111
15 TLMU/IMASK/SEC01      1111_1111_1111_1111_1111_1111_1111_1111
  TLMU/IMASK/SEC02      1111_1111_1111_1111_1111_1111_1111_1111
17 TLMU/IMASK/SEC03      1111_1111_1111_1111_1111_1111_1111_1111
  TLMU/IMASK/SEC04      1111_1111_1111_1111_1111_1111_1111_1111
19 TLMU/IMASK/SEC05      1111_1111_1111_1111_1111_1111_1111_1111
  TLMU/IMASK/SEC06      1111_1111_1111_1111_1111_1111_1111_1111
21 TLMU/IMASK/SEC07      1111_1111_1111_1111_1111_1111_1111_1111
  TLMU/IMASK/SEC08      1111_1111_1111_1111_1111_1111_1111_1111
23 TLMU/IMASK/SEC09      1111_1111_1111_1111_1111_1111_1111_1111
  TLMU/IMASK/SEC10      1111_1111_1111_1111_1111_1111_1111_1111
25 TLMU/IMASK/SEC11      1111_1111_1111_1111_1111_1111_1111_1111
  TLMU/IMASK/SEC12      1111_1111_1111_1111_1111_1111_1111_1111
27 TLMU/IMASK/SEC13      1111_1111_1111_1111_1111_1111_1111_1111
  TLMU/IMASK/SEC14      1111_1111_1111_1111_1111_1111_1111_1111
29 TLMU/IMASK/SEC15      1111_1111_1111_1111_1111_1111_1111_1111
  TLMU/IMASK/SEC17      1111_1111_1111_1111_1111_1111_1111_1111
31
  # How long input if stretched. Value can be 0 to 3
33 TLMU/STRETCH          1

35 # Coincidence matrices set (there are three)
  # (if not set, not activated)
37
  TLMU/CMATRIX0/SEC00 00_0000_0010_0000_0001
39 TLMU/CMATRIX0/SEC01 00_0000_0100_0000_0010
  TLMU/CMATRIX0/SEC02 00_0000_1000_0000_0100
41 TLMU/CMATRIX0/SEC03 00_0001_0000_0000_1000
  TLMU/CMATRIX0/SEC04 00_0010_0000_0001_0000
43 TLMU/CMATRIX0/SEC05 00_0100_0000_0010_0000
  TLMU/CMATRIX0/SEC06 00_1000_0000_0100_0000
45 TLMU/CMATRIX0/SEC07 01_0000_0000_1000_0000
  TLMU/CMATRIX0/SEC08 10_0000_0001_0000_0000
47
```

```

TLMU/CMATRIX1/SEC00 00_0000_0111_0000_0001
49 TLMU/CMATRIX1/SEC01 00_0000_1110_0000_0010
TLMU/CMATRIX1/SEC02 00_0001_1100_0000_0100
51 TLMU/CMATRIX1/SEC03 00_0011_1000_0000_1000
TLMU/CMATRIX1/SEC04 00_0111_0000_0001_0000
53 TLMU/CMATRIX1/SEC05 00_1110_0000_0010_0000
TLMU/CMATRIX1/SEC06 01_1100_0000_0100_0000
55 TLMU/CMATRIX1/SEC07 11_1000_0000_1000_0000
TLMU/CMATRIX1/SEC08 11_0000_0001_0000_0001
57 TLMU/CMATRIX1/SEC09 10_0000_0010_0000_0011
TLMU/CMATRIX1/SEC10 00_0000_0100_0000_0111
59 TLMU/CMATRIX1/SEC11 00_0000_1000_0000_1110
TLMU/CMATRIX1/SEC12 00_0001_0000_0001_1100
61 TLMU/CMATRIX1/SEC13 00_0010_0000_0011_1000
TLMU/CMATRIX1/SEC14 00_0100_0000_0111_0000
63 TLMU/CMATRIX1/SEC15 00_1000_0000_1110_0000
TLMU/CMATRIX1/SEC16 01_0000_0001_1100_0000
65 TLMU/CMATRIX1/SEC17 10_0000_0011_1000_0000

67
TLMU/CMATRIX2/SEC00 00_0000_1111_1000_0001
69 TLMU/CMATRIX2/SEC01 00_0001_1111_0000_0010
TLMU/CMATRIX2/SEC02 00_0011_1110_0000_0100
71 TLMU/CMATRIX2/SEC03 00_0111_1100_0000_1000
TLMU/CMATRIX2/SEC04 00_1111_1000_0001_0000
73 TLMU/CMATRIX2/SEC05 01_1111_0000_0010_0000
TLMU/CMATRIX2/SEC06 11_1110_0000_0100_0000
75 TLMU/CMATRIX2/SEC07 11_1100_0000_1000_0001
TLMU/CMATRIX2/SEC08 11_1000_0001_0000_0011
77 TLMU/CMATRIX2/SEC09 11_0000_0010_0000_0111
TLMU/CMATRIX2/SEC10 10_0000_0100_0000_1111
79 TLMU/CMATRIX2/SEC11 00_0000_1000_0001_1111
TLMU/CMATRIX2/SEC12 00_0001_0000_0011_1110
81 TLMU/CMATRIX2/SEC13 00_0010_0000_0111_1100
TLMU/CMATRIX2/SEC14 00_0100_0000_1111_1000
83 TLMU/CMATRIX2/SEC15 00_1000_0001_1111_0000
TLMU/CMATRIX2/SEC16 01_0000_0011_1110_0000
85 TLMU/CMATRIX2/SEC17 10_0000_0111_1100_0000

87
# Multiplicity counter setup (where to slice) .
89 # there are 9 slices with lower and upper thresholds
TLMU/MCNTR0/THR 5 20
91 TLMU/MCNTR1/THR 20 100
TLMU/MCNTR2/THR 100 200
93 TLMU/MCNTR3/THR 200 300
TLMU/MCNTR4/THR 300 400
95 TLMU/MCNTR5/THR 400 500
TLMU/MCNTR6/THR 500 520
97 TLMU/MCNTR7/THR 520 999
TLMU/MCNTR8/THR 1 576
99

101 # Assign signal to output. CM means CMATRIX and MC means
# Multiplicity counter, SEQ [0..4] means trigger sequencer.
103 # NONE will not assign anything
#

```

```

105 # channel          0  1  2  3  4  5  6  7
    TLMU/OUTMUX      CM1 MC2 MC3 MC4 MC5 MC6 MC7 MC8
107
    # FEBs
109
    # basically thresholds and delay (T0 has 12 channels, and V0 has 8)
111 # V0 has 4 sections named V0, V1, V2, V3
    # Delay is 0 to 31, with 1/4 BC precision (max delay is then 8 BCs)
113 # The values which can be taken here are from 0 to 255 for threshold
    # and 0 to 31 for delay
115
    FEB/T0/A/THR      10 10 10 10 10 10 10 10 10 10 10 10
117 FEB/T0/A/DELAY    1  1  1  1  1  1  1  1  1  1  1  1
    FEB/T0/C/THR      10 10 10 10 10 10 10 10 10 10 10 10
119 FEB/T0/C/DELAY    1  1  1  1  1  1  1  1  1  1  1  1

121 FEB/V0/A0/THR     20 20 20 20 20 20 20 20
    FEB/V0/A1/THR     20 20 20 20 20 20 20 20
123 FEB/V0/A2/THR     20 20 20 20 20 20 20 20
    FEB/V0/A3/THR     20 20 20 20 20 20 20 20
125
    FEB/V0/A0/DELAY    1  1  1  1  1  1  1  1
127 FEB/V0/A1/DELAY    1  1  1  1  1  1  1  1
    FEB/V0/A2/DELAY    1  1  1  1  1  1  1  1
129 FEB/V0/A3/DELAY    1  1  1  1  1  1  1  1

131 FEB/V0/C0/THR     20 20 20 20 20 20 20 20
    FEB/V0/C1/THR     20 20 20 20 20 20 20 20
133 FEB/V0/C2/THR     20 20 20 20 20 20 20 20
    FEB/V0/C3/THR     20 20 20 20 20 20 20 20
135
    FEB/V0/C0/DELAY    1  1  1  1  1  1  1  1
137 FEB/V0/C1/DELAY    1  1  1  1  1  1  1  1
    FEB/V0/C2/DELAY    1  1  1  1  1  1  1  1
139 FEB/V0/C3/DELAY    1  1  1  1  1  1  1  1

141 # Lookup table at FEB

143 FEB/T0/A/LUT/0    M(1111_1111_1111)>0 # maybe also logical equations
    FEB/T0/A/LUT/1    M(1111_1111_1111)>4
145
    FEB/V0/A0/LUT/0    M(1111_1111)>0
147 FEB/V0/A0/LUT/1    M(1111_1111)>2
    FEB/V0/A1/LUT/0    M(1111_1111)>0
149 FEB/V0/A1/LUT/1    M(1111_1111)>2
    FEB/V0/A2/LUT/0    M(1111_1111)>0
151 FEB/V0/A2/LUT/1    M(1111_1111)>2
    FEB/V0/A3/LUT/0    M(1111_1111)>0
153 FEB/V0/A3/LUT/1    M(1111_1111)>2

155 FEB/T0/C/LUT/0    M(1111_1111_1111)>0
    FEB/T0/C/LUT/1    M(1111_1111_1111)>4
157
    FEB/V0/C0/LUT/0    M(1111_1111)>0
159 FEB/V0/C0/LUT/1    M(1111_1111)>2
    FEB/V0/C1/LUT/0    M(1111_1111)>0
161 FEB/V0/C1/LUT/1    M(1111_1111)>2

```

```

FEB/V0/C2/LUT/0      M(1111_1111)>0
163 FEB/V0/C2/LUT/1      M(1111_1111)>2
    FEB/V0/C3/LUT/0      M(1111_1111)>0
165 FEB/V0/C3/LUT/1      M(1111_1111)>2

167 # Lookup table at CB-AC

169 CBA/LUT/0      T0_1 || ( V0-0_1 || V0-1_1 || V0-2_1 || V0-3_1 )
    CBA/LUT/1      !T0_0 && !V0-0_0 && !V0-1_0 && !V0-2_0 && !V0-3_0
171
    CBC/LUT/0      T0_1 || ( V0-0_1 || V0-1_1 || V0-2_1 || V0-3_1 )
173 CBC/LUT/1      !T0_0 && !V0-0_0 && !V0-1_0 && !V0-2_0 && !V0-3_0

175 # Lookup table at CB-B

177 CBB/LUT/0      CB-A_1 && !CB-C_1 && TLMU_7
    CBB/LUT/1      !CB-A_1 && CB-C_1 && TLMU_7
179 CBB/LUT/2      ( CB-A_1 && CB-C_1 ) && TLMU_7

181 # Timing parameter for trigger processor

183 CBB/TRG/L0A      43 # comment
    CBB/TRG/L0S      47
185 CBB/TRG/L1A      308
    CBB/TRG/L1S      311
187 CBB/TRG/DEAD/PT  200
    CBB/TRG/DEAD/L0  350
189 CBB/TRG/DEAD/L1  500
    CBB/TRG/DELAY/L0 46
191
    CBB/TRG/CTRL/SM_TO_CTP YES
193 CBB/TRG/CTRL/TRG_EMU YES
    CBB/TRG/CTRL/A/VALUE 0
195 CBB/TRG/CTRL/A/OVR NO
    CBB/TRG/CTRL/B/VALUE 0
197 CBB/TRG/CTRL/B/OVR NO

199 CBB/TRG/A/DIS    YES # do not change!

201 CBB/TRG/TIN/0    0 # normal triggering (should be 0!)
    CBB/TRG/TIN/1    0 # normal triggering (should be 0!)
203
    CBB/PT/CBA/SAMPL 0
205 CBB/PT/CBC/SAMPL 0

207
    CBB/PT/ALIGN/CB-A_0/STRETCH 0
209 CBB/PT/ALIGN/CB-A_0/DELAY 0
    CBB/PT/ALIGN/CB-A_1/STRETCH 0
211 CBB/PT/ALIGN/CB-A_1/DELAY 0
    CBB/PT/ALIGN/CB-C_0/STRETCH 0
213 CBB/PT/ALIGN/CB-C_0/DELAY 0
    CBB/PT/ALIGN/CB-C_1/STRETCH 0
215 CBB/PT/ALIGN/CB-C_1/DELAY 0
    CBB/PT/ALIGN/RND/STRETCH 0
217 CBB/PT/ALIGN/RND/DELAY 0
    CBB/PT/ALIGN/BC/STRETCH 0

```

```

219 CBB/PT/ALIGN/BC/DELAY      0
    CBB/PT/ALIGN/TLMU_0/STRETCH 0
221 CBB/PT/ALIGN/TLMU_0/DELAY  0
    CBB/PT/ALIGN/TLMU_1/STRETCH 0
223 CBB/PT/ALIGN/TLMU_1/DELAY  0
    CBB/PT/ALIGN/TLMU_2/STRETCH 0
225 CBB/PT/ALIGN/TLMU_2/DELAY  0
    CBB/PT/ALIGN/TLMU_3/STRETCH 0
227 CBB/PT/ALIGN/TLMU_3/DELAY  0
    CBB/PT/ALIGN/TLMU_4/STRETCH 0
229 CBB/PT/ALIGN/TLMU_4/DELAY  0
    CBB/PT/ALIGN/TLMU_5/STRETCH 0
231 CBB/PT/ALIGN/TLMU_5/DELAY  0
    CBB/PT/ALIGN/TLMU_6/STRETCH 0
233 CBB/PT/ALIGN/TLMU_6/DELAY  0
    CBB/PT/ALIGN/TLMU_7/STRETCH 0
235 CBB/PT/ALIGN/TLMU_7/DELAY  0
    CBB/PT/ALIGN/CB-B_0/STRETCH 0
237 CBB/PT/ALIGN/CB-B_0/DELAY  0
    CBB/PT/ALIGN/CB-B_1/STRETCH 0
239 CBB/PT/ALIGN/CB-B_1/DELAY  0

241 CBB/BUSY/CTRL              0

243 CBB/RND/THR                 150000
    CBB/BC/RESET.VALUE         222
245
    CBB/PT/MASK/CB-A_0         YES
247 CBB/PT/MASK/CB-A_1         NO
    CBB/PT/MASK/CB-C_0         YES
249 CBB/PT/MASK/CB-C_1         NO
    CBB/PT/MASK/RND            NO
251 CBB/PT/MASK/BC             NO
    CBB/PT/MASK/TLMU_0         YES
253 CBB/PT/MASK/TLMU_1         YES
    CBB/PT/MASK/TLMU_2         YES
255 CBB/PT/MASK/TLMU_3         YES
    CBB/PT/MASK/TLMU_4         YES
257 CBB/PT/MASK/TLMU_5         YES
    CBB/PT/MASK/TLMU_6         YES
259 CBB/PT/MASK/TLMU_7         YES
    CBB/PT/MASK/CB-B_0         YES
261 CBB/PT/MASK/CB-B_1         YES
    CBB/PT/MASK/CB-B_2         YES
263
    # EOF

```


Acknowledgments

Special thanks go to Prof. Dr. Johanna Stachel, giving me the opportunity to carry out my bachelor thesis and to obtain an insight in high-energy particle physics.

I would like to thank Prof. Dr. Peter Glässel for reading and evaluating my thesis. Dr. Rainer Schicker deserves many thanks for guiding and supporting me during my thesis.

I am very grateful for Dr. Kai Schweda's introduction to the life at CERN (as well as Point 2 and the TRD house), his help in a lot of situations and reading my thesis. I wish to express my gratitude to Dr. Ken Oyama, Bastian Bathen, Jochen Klein, Jörg Lehnert and the whole pre-trigger team for all the discussions and meetings which taught me a lot.

I would like to thank Jochen Klein for his help with AliRoot and pre-trigger specific problems.

I greatly appreciate the help of Dr. Paul Constantin and PD Dr. Klaus Reygers with the fits.

Last not least, I would like to express my thanks to all people in the group providing such a kind working atmosphere and help: Friederike Bock, Maren Hellwig, Mustapha Al-Helwi, Dr. Oliver Busch, Daniel Lohner, Michael Winn and many more.

Bibliography

- [1] D. J. Gross and F. Wilczek. Ultraviolet behavior of non-abelian gauge theories. *Phys. Rev. Lett.*, 30(26):1343–1346, Jun 1973.
- [2] H. D. Politzer. Reliable perturbative results for strong interactions? *Phys. Rev. Lett.*, 30(26):1346–1349, Jun 1973.
- [3] U. Amaldi, M. Jacob, and G. Matthiae. Diffraction of hadronic waves. *Annual Review of Nuclear Science*, 26:385–456, December 1976.
- [4] TOTEM cross section: Elastic scattering and diffraction dissociation at the LHC. CERN-LHCC-97-49.
- [5] V. Barone and E. Predazzi. *High-Energy Particle Diffraction*. Springer, 1. edition, 2002.
- [6] L.A. Harland-Lang, V.A. Khoze, M.G. Ryskin, and W.J. Stirling. Central exclusive χ_c meson production at the Tevatron revisited. 2009, hep-ph/0909.4748v2.
- [7] T. Akesson et al. (The Axial Field Spectrometer Collaboration). A search for glueballs and a study of double pomeron exchange at the CERN Intersecting Storage Rings. *Nucl. Phys. B*, 264:154–194, 1986.
- [8] Y. Chen et al. Glueball spectrum and matrix elements on anisotropic lattices. *Phys. Rev.*, D73:014516, 2006, hep-lat/0510074.
- [9] V. Crede and C. A. Meyer. Experimental status of glueballs. Mar 2009, hep-ph/0812.0600v3.
- [10] L.A. Harland-Lang, V.A. Khoze, M.G. Ryskin, and W.J. Stirling. Standard candle central exclusive processes at the Tevatron and LHC. 2010, hep-ph/1005.0695v1.
- [11] C. Amsler et al. (Particle Data Group). Note on branching ratios of $\psi(2s)$ and $\chi_c(0, 1, 2)$. *Phys. Lett. B*667, page 1, 2008.
- [12] P. González, P. Ladrón de Guevara, E. López Torres (3), A. Marín, and E. Seradilla. Simulation study of $\chi_c \rightarrow j/\psi + \gamma$ detection with $j/\psi \rightarrow e^+e^-$ in pp collisions. *Eur.Phys.J.C*9, 61:899–903, 2009.
- [13] A. Breakstone et al. Measurement of $p\bar{p}$ and pp elastic scattering in the dip region at $\sqrt{s} = 53$ GeV. *Phys. Rev. Lett.*, 54(20):2180–2183, May 1985.
- [14] S. J. Brodsky, J. Rathsmann, and C. Merino. Odderon-pomeron interference. *Phys. Lett.*, B461:114–122, 1999, hep-ph/9904280.

- [15] K. Aamodt et al. (The ALICE Collaboration). The ALICE experiment at the CERN LHC. *JINST*, 3:08002, 2008.
- [16] S. Abreu et al. Heavy ion collisions at the LHC - last call for predictions. *Journal of Physics G: Nuclear and Particle Physics*, 35(5):054001, 2008, hep-ph/0711.0974v1.
- [17] J. Alme et al. The ALICE TPC, a large 3-dimensional tracking device with fast readout for ultra-high multiplicity events. 2010, physics.ins-det/1001.1950v1.
- [18] F.W. Bopp, R. Engel, and J. Ranft. Rapidity gaps and the PHOJET Monte Carlo, version 1.12-35. arXiv:hep-ph/9803437.
- [19] R. Engel, J. Ranft, and S. Roesler. Hard diffraction in hadron-hadron interactions and in photoproduction. *Phys. Rev.*, D52:1459, 1995.
- [20] R. Schicker. The ALICE detector and trigger strategy for diffractive and electromagnetic processes. *Nuclear Physics B - Proceedings Supplements*, 179-180:196 – 201, 2008. Proceedings of the International Workshop on High-Energy Photon Collisions at the LHC.
- [21] ROOT Homepage. <http://root.cern.ch>, May 2010.
- [22] T. Sjöstrand, S. Mrenna, and P. Skands. PYTHIA 6.4 physics and manual; v6.420, tune ATLAS. *JHEP*, 05:026, 2006.
- [23] AliEn. <http://alien2.cern.ch>, May 2010.
- [24] Worldwide LHC Computing Grid website. <http://lcg.web.cern.ch/LCG/>.
- [25] Alice-Collaboration. AliRoot Documentation — Alice Offline pages. <http://aliweb.cern.ch/Offline/AliRoot/Manual.html>, May 2010.
- [26] B. Bathen. *PhD thesis under preparation*. PhD thesis, University of Muenster, 2010.
- [27] T. Dietel, J. Klein, K. Oyama, and K. Schweda. *TRD Documentation Project*, May 2010.
- [28] T. Sjöstrand. Pythia8 documentation. <http://home.thep.lu.se/~torbjorn/pythiaaux/present.html>, May 2010.
- [29] E. Gotsman, E. Levin, and U. Maor. A QCD motivated model for soft interactions at high energies. May 2005, hep-ph/0805.2799v2.
- [30] M.G. Ryskin, A.D. Martin, and V.A. Khoze. Soft diffraction at the LHC: a partonic interpretation. *Eur.Phys.J.*, C54:199, 2008.
- [31] U. Maor. The interplay between data and theory in recent unitary models. Nov 2008, hep-ph/0811.2636v1.

Erklärung:

Ich versichere, dass ich diese Arbeit selbständig verfasst habe und keine anderen als die angegebenen Quellen und Hilfsmittel benutzt habe.

Heidelberg, den 10. Juni 2010

Unterschrift:
Felix Reidt